Brick wall in an AdS-Schwarzschild black hole: Normal modes and emerging thermality

Suman Das,[1,*] Somnath Porey,[2,†] and Baishali Roy[2,‡]

[1]*Theory Division, Saha Institute of Nuclear Physics, A CI of Homi Bhabha National Institute, 1/AF, Bidhannagar, Kolkata 700064, India*

[2]*Ramakrishna Mission Vivekananda Educational and Research Institute, Belur Math, Howrah-711202, West Bengal, India*

(Received 19 April 2025; accepted 10 October 2025; published 24 November 2025)

This paper investigates the normal modes of a probe scalar field in a five-dimensional AdS-Schwarzschild black hole with the brick wall boundary condition near the horizon. We employ various techniques to compute the spectrum and analyze its properties. Our results reveal a linear dependence of the spectrum on the principal quantum number while demonstrating a nontrivial dependence on the angular momentum quantum number. We compute the spectral form factor (SFF) and find a dip-ramp-plateau structure, with the slope of the ramp approaching unity as the brick wall nears the horizon. This feature appears to vanish when the horizon size becomes much larger compared to the anti–de Sitter length. We also observe that as the brick wall approaches the horizon, the poles of the retarded Green's function condense on the real line, leading to an emergent thermal behavior in the boundary theory. This work extends previous studies on lower-dimensional black holes to higher dimensions, providing insights into the connection between black hole microstate models and boundary chaos. Our findings contribute to the ongoing discussions on the information paradox and the nature of black hole interiors in the context of anti–de Sitter/conformal field theory correspondence.

DOI: 10.1103/dqnb-kg1z

I. INTRODUCTION

Strongly interacting theories are generally chaotic. While chaos in classical mechanics is well defined, its counterpart in the quantum world is less clear. Various attempts have been made to bridge these two realms at the semiclassical level [1–4], but a comprehensive understanding remains elusive. Over the years, several measures have been developed to quantify quantum chaos, yet ambiguity persists. One notable measure is the out-of-time-ordered correlator (OTOC) [5,6], which measures early time chaos, whereas the spectral form factor (SFF) [7,8] measures chaos at late times. Level spacing distribution (LSD) has also been a valuable tool for understanding quantum chaos since the pioneering work of Wigner and Dyson [9,10]. Although strongly interacting systems are intriguing, they are notoriously difficult to solve. This is where random matrix theory (RMT) universality provides critical insights into the statistical properties of these systems. RMT is universal in the sense that the symmetry class of the Hamiltonian determines the ensemble of the random matrix theory, offering a powerful framework for analyzing complex quantum systems.

Thermality is intrinsically linked with chaos, and it is both intriguing and challenging to understand how thermality arises in a closed, isolated system. Though there are several ideas to support this, including typicality and the concept of a bath (see [11] for details), the satisfactory mechanism is not yet well understood. One such mechanism is provided by the eigenstate thermalization hypothesis (ETH) [11,12]. Furthermore, for a pure state with very large entropy (e.g., large N), quantum statistical mechanics shows that the variance of any local correlation function is suppressed by a factor of e^{-S} [13], where S can be identified as the entropy. Therefore, in a strongly interacting system with a large number of degrees of freedom, it is possible that the low-point correlation function can be well approximated by its thermal expectation value.

At first glance, the concepts discussed above may seem disconnected, but they are closely related to black holes and quantum gravity. The AdS/CFT correspondence [14] offers a framework that links an interacting conformal field theory (CFT) with quantum gravity in anti–de Sitter (AdS)

*Contact author: suman.das@saha.ac.in
†Contact author: somnathhimu00@gm.rkmvu.ac.in
‡Contact author: baishali.roy025@gm.rkmvu.ac.in

Published by the American Physical Society under the terms of the Creative Commons Attribution 4.0 International license. Further distribution of this work must maintain attribution to the author(s) and the published article's title, journal citation, and DOI. Funded by SCOAP³.

spacetime. Since its inception, AdS/CFT has provided numerous insights that have deepened our understanding of black holes and their semiclassical properties [15–22]. However, the questions of smoothness of the horizon and the existence of an interior remain unresolved [23,24]. This smoothness is at the heart of the information paradox [23,25,26]. Despite notable recent progress [27,28], the paradox remains unresolved, especially in the Lorentzian picture and for the higher-dimensional black holes.

On the other hand, string theory provides alternatives such as fuzzballs which can bypass this. According to the fuzzball proposal, the horizon is not a smooth place and must be replaced by a complex stringy structure [29–32]. For some particular cases, there exists a whole moduli space of such solutions which, when quantized and counted, give rise to perfect agreement with the Bekenstein-Hawking entropy of the black hole [33,34]. Another interesting fact is that, in the low-energy supergravity limit, many of these solutions can be written as explicit metrics called microstate geometries (see [35] for a review). These are perfectly regular geometries and behave similarly to black holes from a distance, but cap off smoothly near the horizon. Although there are many criticisms (e.g., [36]) regarding the geometric picture, the main takeaway (for our purpose) is that string theory (as a UV-complete theory) can provide mechanisms that support a structure near the horizon.[1]

Black holes are expected to be chaotic objects as their boundary duals are strongly coupled interacting theories. This can be seen by computing the out-of-time-order correlators (OTOCs) in black hole geometries [6,19]. Moreover, it has been shown that black holes are maximally chaotic in the sense that the Lyapunov exponent saturates the chaos bound,

$$\lambda = \frac{2\pi}{\beta}, \tag{1}$$

where β is the inverse Hawking temperature of the black hole. It is important to remember that OTOCs measure early time chaos, and there is evidence (e.g., [39]) that early time chaos does not always imply chaos for all times. This raises the question: How can we demonstrate that the system remains chaotic at late times? Tools such as the SFF and LSD require knowledge of the spectrum, necessitating the quantization of the black hole system—a challenging problem.[2] A simpler and more tractable question might be: Can we detect any hint of late-time chaos in the probe sector?

A naive probe calculation results in complex-valued quasinormal modes, leading to a vanishing SFF at late times, a manifestation of the information paradox as discussed in [15]. To circumvent this problem, [40,41] proposed placing a brick wall in the geometry[3] and quantizing a probe scalar field to obtain normal modes as a function of the wall's position. It was shown that when the brick wall is placed very near to the horizon, the SFF constructed from these normal modes exhibits a clear dip-ramp-plateau structure with a linear ramp of slope one in the log-log plot. Although the LSD is not of the Wigner-Dyson type (despite exhibiting level repulsion), a WD-type LSD was achieved by imposing fluctuations in the stretched horizon, which may be natural in constructing a more realistic toy version of actual fuzzballs [41]. This approach was generalized for rotating BTZ geometry in [43]. It has been argued in [40,41] that this behavior is a generic feature of any nonextremal black hole, with supporting calculations in the Rindler $\times S^1$ framework. However, no explicit calculations have been performed for higher-dimensional black holes. This article fills this gap by computing the normal modes of a probe scalar field in a five-dimensional AdS Schwarzschild black hole.

This study is intriguing for several reasons. First, in three dimensions, gravity is nondynamical as the degrees of freedom of the graviton are zero, whereas in higher dimensions, gravity is fully dynamical. Second, the AdS/CFT correspondence is much better understood for $\mathrm{AdS}_5 - \mathrm{CFT}_4$. For example, the CFT is a $3+1$ dimensional $\mathcal{N}=4$ super Yang-Mills (SYM) theory, where the glueball operators $\mathrm{Tr}(F_{\mu\nu}F^{\mu\nu})$ and $\mathrm{Tr}(F_{\mu\nu}\tilde{F}^{\mu\nu})$ are dual to the dilaton and axions, which are minimally coupled scalar fields in the bulk AdS. Thus, we can relate the bulk results to a more realistic four-dimensional strongly interacting theory.

The organization of the paper is as follows: In the next section (Sec. II), we describe the setup and identify the radial equation as the Heun equation. Subsequently, we attempt to solve the Heun equation using different methods and extract the normal modes. In Sec. III, we leverage the fact that the BPZ equation in Liouville CFTs also satisfies the Heun equation. By using crossing symmetries, one can relate the solutions around different singular points. Using the solutions around different singular points, we first compute the quasinormal modes with the ingoing boundary condition in Sec. III A, and then extract the normal modes in Sec. III B. In Sec. IV, we use the WKB approximation method to find the normal modes with Dirichlet boundary conditions on the probe field near the horizon. Additionally, we demonstrate that the SFF in this case

[1]Notably, long ago, 't Hooft considered an ad-hoc model [37] by placing a brick wall at a Planck distance away from the horizon and quantizing scalar fields in this geometry, which reproduced the entropy as a one-loop effect (see also [38] for a microcanonical version of the same).

[2]In two-dimensional JT gravity, which is dual to the SYK model, it has been shown that the SFF exhibits a linear ramp with a slope of one, and the LSD follows the Wigner-Dyson distribution [8].

[3]This is motivated by the fuzzball picture. Note that most actual fuzzball geometries are for extremal black holes, making the notion of chaos less meaningful there (see [42] for recent progress).

exhibits a dip-ramp-plateau behavior, with the slope of the ramp approaching one as the Dirichlet wall moves closer to the horizon. In Sec. V, we use another perturbative method to solve the Heun equation and compute the normal modes. In Sec. VI, we show the emergence of a branch cutlike structure in the Green's function of the probe field as the wall is moved closer to the horizon. Finally, in Sec. VII, we conclude with a discussion and outline a few possible future directions. Additionally, we have provided three Appendices A, B, and C to make the paper self-contained.

II. THE SETUP: SCALAR FIELD IN ADS SCHWARZSCHILD BLACK HOLE

Let us consider a probe scalar field of mass μ in the five-dimensional AdS-Schwarzschild black hole geometry,

$$ds^2 = -f(r)dt^2 + \frac{dr^2}{f(r)} + r^2 d\Omega_3^2, \tag{2}$$

with $f(r) = (1 - \frac{r_H^2}{r^2})(r^2 + r_H^2 + 1)$, where r_H represents the position of the horizon (we have set the AdS length l to 1). The mass of the black hole, M is related to the horizon as,

$$r_H^2 = \frac{1}{2}\left(\sqrt{1 + \frac{32 G_N M}{3\pi}} - 1\right). \tag{3}$$

As mentioned in the introduction, our measuring probe is a scalar field Φ in this black hole background which satisfies the following Klein-Gordon equation:

$$\Box\Phi \equiv \frac{1}{\sqrt{|g|}}\partial_\nu(\sqrt{|g|}\partial^\nu\Phi) = \mu^2\Phi. \tag{4}$$

Where μ is the mass associated with the scalar field. The conformal dimension of the boundary operator dual to Φ is given by,

$$\mu = \sqrt{\Delta(\Delta - 4)}. \tag{5}$$

Since the metric is time-independent and spherically symmetric, we can use the ansatz

$$\Phi(t, r, \Omega) \sim e^{-i\omega t} Y_{l,\vec{m}}(\Omega)\phi_{\omega l}(r), \tag{6}$$

where $Y_{l,\vec{m}}(\Omega)$ represent spherical harmonics on S^3. These harmonics satisfy the following equation:

$$\nabla^2_{S^3} Y_{l,\vec{m}} = -l(l+2)Y_{l,\vec{m}}, \tag{7}$$

where $\nabla^2_{S^3}$ is the Laplacian on S^3 and $\vec{m} = (m, m')$ can go from $-l/2$ to $l/2$ (see [44]). With this, (4) can be written as [to simplify our notation, we will now write $\phi_{\omega l}(r)$ as $\phi(r)$],

$$\frac{1}{r^3}\frac{d}{dr}\left(r^3 f(r)\frac{d\phi(r)}{dr}\right) + \left(\frac{\omega^2}{f(r)} - \frac{l(l+2)}{r^2} - \mu^2\right)\phi(r) = 0. \tag{8}$$

This is a Heun's equation which can be written in the well-known normal form by using the following transformations,

$$z = \frac{r^2}{r_H^2 + r^2 + 1}, \tag{9}$$

$$\phi(r) = z^{-\frac{1}{2}}(z - \tilde{t})^{-\frac{1}{2}}(1 - z)^{\frac{1}{2}}\chi(z). \tag{10}$$

In this new z coordinate, the horizon is located at $z = \tilde{t} = \frac{r_H^2}{2r_H^2+1}$ and the boundary is at $z = 1$. The radial equation is,

$$\left(\partial_z^2 + \frac{\frac{1}{4} - a_1^2}{(z-1)^2} - \frac{\frac{1}{2} - a_0^2 - a_1^2 - a_{\tilde{t}}^2 + a_\infty^2 + u}{z(z-1)} + \frac{\frac{1}{4} - a_{\tilde{t}}^2}{(z-\tilde{t})^2} + \frac{u}{z(z-\tilde{t})} + \frac{\frac{1}{4} - a_0^2}{z^2}\right)\chi(z) = 0. \tag{11}$$

The various parameters appearing in Eq. (11) are detailed in Appendix C.

Near horizon behavior of $\chi(z)$ is the following

$$\begin{aligned}\chi_{\text{hor}}(z) &= c_1(\tilde{t} - z)^{\frac{1}{2}+a_{\tilde{t}}} + c_2(\tilde{t} - z)^{\frac{1}{2}-a_{\tilde{t}}} + \ldots \\ &= c_1\chi_+^{(\tilde{t})}(z) + c_2\chi_-^{(\tilde{t})}(z) + \ldots\end{aligned} \tag{12}$$

Here, the first term corresponds to the outgoing mode and the second term to the ingoing mode near the horizon. The constants c_1 and c_2 are arbitrary. Similarly, near boundary behavior can be expressed as,

$$\begin{aligned}\chi_{\text{bdry}}(z) &= c_3\left(\frac{1-z}{1+r_H^2}\right)^{\frac{1}{2}+a_1} + c_4\left(\frac{1-z}{1+r_H^2}\right)^{\frac{1}{2}-a_1} + \ldots \\ &= c_3\chi_+^{(1)}(z) + c_4\chi_-^{(1)}(z) + \ldots\end{aligned} \tag{13}$$

Where the first term corresponds to the normalizable mode and the second term is non-normalizable.

Since the radial equation is a Heun's equation, a closed-form solution in terms of known functions is not available. However, we can still use techniques from Liouville CFT to write the connection formulas that relate the solutions around various singular points. These connection formulas will aid us in finding the normal modes, as we will discuss in the next section.

III. USING EXPLICIT CONNECTION FORMULAS

In Liouville CFT, the BPZ equation reduces to Heun's equation in normal form in the semiclassical limit.

The solutions of this equation correspond to conformal blocks associated with different channels. By using the crossing symmetries of the conformal blocks, we can determine the relations between solutions around different singular points [45], which provide the required connection formulas. As noted in the previous section, the radial Eq. (8) satisfied by the probe scalar field in five-dimensional AdS–Schwarzschild geometry takes the form of a Heun equation. We can therefore exploit the previously discussed connection formulas to determine the normal modes[4] in the AdS-Schwarzschild brickwall geometry.

As a warm-up let us first focus on the computation of quasinormal modes and the Green's function in the AdS-Schwarzschild black hole metric.

A. Ingoing boundary condition and quasinormal modes

The natural boundary condition near the horizon of a black hole is ingoing boundary condition which implies $c_1 = 0$. So,

$$\chi_{\rm hor}(z) = c_2 \chi_-^{(\tilde{t})}(z). \tag{14}$$

Using the connection formulas, we can write the near-horizon solution in terms of the solution near the boundary. Let us write the relations between the near-horizon and near-boundary solutions in the following way[5]:

$$\chi_+^{(\tilde{t})} = a_{11}\chi_+^{(1)} + a_{22}\chi_-^{(1)}, \tag{15}$$

$$\chi_-^{(\tilde{t})} = b_{11}\chi_+^{(1)} + b_{22}\chi_-^{(1)}. \tag{16}$$

Using (15) in (14), we get

$$\chi_{\rm hor}(z) = c_2(b_{11}\chi_+^{(1)} + b_{22}\chi_-^{(1)}). \tag{17}$$

To find the quasinormal modes we need to impose normalizablity at the boundary, which implies,[6]

$$b_{22} = M_{-+}(a_{\tilde{t}}, a; a_0)M_{--}(a, a_1; a_\infty) + M_{--}(a_{\tilde{t}}, a; a_0)M_{+-}(a, a_1; a_\infty)\tilde{t}^{-2a}e^{\partial_a F} = 0. \tag{18}$$

This can be solved to extract the quasinormal modes of the black hole (see [46,47] for the details). Following the Son-Starinets prescription [48], the retarded Green's function can be expressed as the ratio of the normalizable to non-normalizable modes as follows,

$$G_R^{\rm BH}(\omega, \lambda) = \frac{b_{11}}{b_{22}}. \tag{19}$$

B. Dirichlet boundary condition and normal modes

Instead of imposing an ingoing boundary condition near the horizon, we now consider the Dirichlet boundary condition $\Phi(z_0) = 0$ at some $z_0 > \tilde{t}$. This boundary condition is motivated by the desire to connect the brick wall-type model of 't Hooft with the fuzzball (microstate geometry) picture. It is important to note that, in principle, the brick wall can be placed at any location since it is an *ad hoc* boundary condition within the realm of classical general relativity. However, as noted in works by 't Hooft [37] and [38,40,41,49,50], interesting physics emerges when the brick wall is very close to the horizon. Therefore, we take $z_0 \to \tilde{t}$. In this region Dirichlet boundary condition implies,

$$\chi_{\rm hor}(z_0) = c_1\chi_+^{(\tilde{t})}(z_0) + c_2\chi_-^{(\tilde{t})}(z_0) = 0, \tag{20}$$

which implies,

$$R_{c_1c_2} = \frac{c_1}{c_2} = -\frac{\chi_-^{(\tilde{t})}(z_0)}{\chi_+^{(\tilde{t})}(z_0)} = -\frac{(\tilde{t}-z_0)^{\frac{1}{2}-a_{\tilde{t}}}}{(\tilde{t}-z_0)^{\frac{1}{2}+a_{\tilde{t}}}} = -(\tilde{t}-z_0)^{-2a_{\tilde{t}}}. \tag{21}$$

Then the near-horizon solution comes out to be,

$$\chi^{(\tilde{t})}(z) = c_2(R_{c_1c_2}\chi_+^{(\tilde{t})}(z) + \chi_-^{(\tilde{t})}(z)). \tag{22}$$

Using (15) in (22), we can relate the near-horizon and near-boundary solutions as follows:

$$\chi^{(\tilde{t})} = c_2((R_{c_1c_2}a_{11} + b_{11})\chi_+^{(1)} + (R_{c_1c_2}a_{22} + b_{22})\chi_-^{(1)}). \tag{23}$$

Then normalizable condition at the boundary implies,

$$R_{c_1c_2}a_{22} + b_{22} = 0. \tag{24}$$

Substituting (21) in (24),

$$\frac{b_{22}}{a_{22}} = (\tilde{t}-z_0)^{-i\omega\frac{r_H}{1+2r_H^2}} = \epsilon_0^{-i\omega\frac{r_H}{1+2r_H^2}}. \tag{25}$$

Here ϵ_0 measures the distance between the horizon and the brick wall. In Appendix C, we have shown that the absolute value of $\frac{b_{22}}{a_{22}}$ is always one, i.e., the absolute part is trivially

[4]Typically solving for a probe scalar field in black hole geometries involves imposing ingoing boundary conditions at the horizon, leading to quasinormal modes. In contrast, the brick wall model imposes reflective boundary conditions near the horizon, resulting in normal modes instead.

[5]The exact expressions of a_{11}, a_{22}, b_{11}, and b_{22} are given in the Appendix C.

[6]Functional form of the connection matrix $M_{\theta\theta'}$ and the prepotential F appearing in this equation is given in Appendix C.

satisfied.[7] Therefore, what we have is the argument part, which is

$$\mathrm{Arg}\left(\frac{b_{22}}{a_{22}}\right) = \mathrm{Arg}\left(\epsilon_0^{-i\omega\frac{r_H}{1+2r_H^2}}\right) + \mathrm{Arg}(1), \tag{26}$$

which can be simplified as,

$$\mathrm{Arg}\left(\frac{b_{22}}{a_{22}}\right) + \frac{\omega r_H}{(1+2r_H^2)}\log\epsilon_0 = 2n\pi, \quad \text{where } n \in \mathbf{Z}. \tag{27}$$

The solution of this equation provides the required normal modes, which are real valued and labeled by two quantum numbers, n and l. We have solved this equation using *Mathematica*. The behavior of the normal modes along the l and n directions is presented in Fig. 1. Although the spectrum exhibits a nontrivial dependence on the l-quantum number, along the n direction it is almost linear, as observed for the BTZ black hole in [40]. The figure clearly shows that the dependence of the modes on the l-direction is much slower compared to the n-direction. This quasidegeneracy along l-directions is the key feature that underpins the emergence of interesting nontrivial physics. The corresponding spectral form factor (SFF) [see Appendix A for the definition] is presented in Fig. 2. Unlike the BTZ case, the SFF for the modes along the l-direction does not exhibit a linear ramp. This deviation arises from the absence of logarithmic growth in the low-lying modes of the spectrum along l. The observed l-dependence of the modes raises a natural question: why do these modes differ significantly from those of the BTZ black hole in [40,43]? This difference is not primarily due to the change in dimensionality (from 3D to 5D spacetime) but is instead attributed to the condition $r_H \gg l$. To substantiate this claim, a comparative plot is provided in Fig. 3.

In Fig. 4 (left), we present the Δ dependence of the normal modes along l-direction. For smaller values of l, ω varies significantly with different Δ. However, as l increases, these differences gradually diminish, and the modes tend to converge onto a single curve. A similar trend is observed for the normal modes of the BTZ black hole, as depicted on the right of Fig. 4. Notably, there is a key difference between the two cases: in the BTZ black hole, the modes increase with increasing $\Delta > d$, whereas for the AdS-Schwarzschild black hole, the opposite trend is observed, with the modes decreasing as Δ increases.

Due to the complexity of the various functions appearing in (27), we were unable to solve for larger values of l and n and also for smaller value of r_H/l. More advanced numerical techniques are required to extend the solution to larger l and n. Nonetheless, we can explore various approximate methods to solve the radial equation, as discussed in the next two sections.

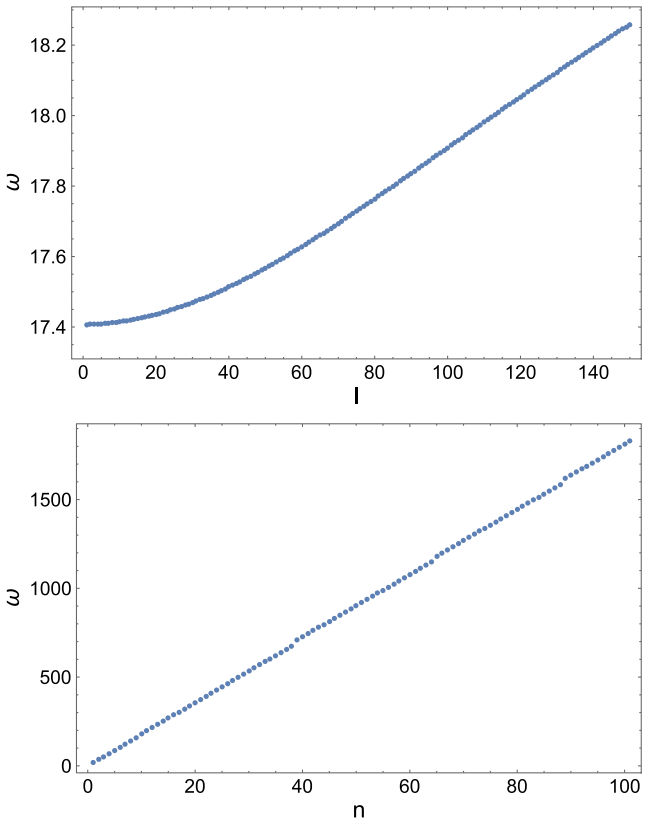


FIG. 1. Spectrum along l (left) and n (right) directions obtained by solving (27). The parameters used are $r_H = 100, \Delta = 4.1$ and $\epsilon_0 = 10^{-30}$. Although the spectrum has a trivial linear dependence on n-quantum number, along l direction it is nontrivial.

IV. WKB APPROXIMATION METHOD

In this section we will try to solve the radial equation using the WKB method.[8] For this, we will write (8) in Schrödinger form to get an effective potential, and then we will find the bound states of the potential which will essentially correspond to the normal modes of the scalar perturbation.

In general, an equation of the following form,

$$a(r)\frac{d^2\phi(r)}{dr^2} + b(r)\frac{d\phi(r)}{dr} + c(r)\phi(r) = 0, \tag{28}$$

can be written in the form of Schrödinger equation (with $\phi(r) = g(r)\psi(r)$) as,

$$\frac{d^2\psi(r)}{dr^2} - V(r)\psi(r) = 0, \tag{29}$$

[7](25) can be written as $\frac{b_{22}}{a_{22}}\epsilon_0^{i\omega\frac{r_H}{1+2r_H^2}} = 1$, where the left-hand side is a pure phase and can be labeled as $e^{-i\theta(\omega,l)} = 1$.

[8]For a review of the WKB approximation method, look into Appendix B.

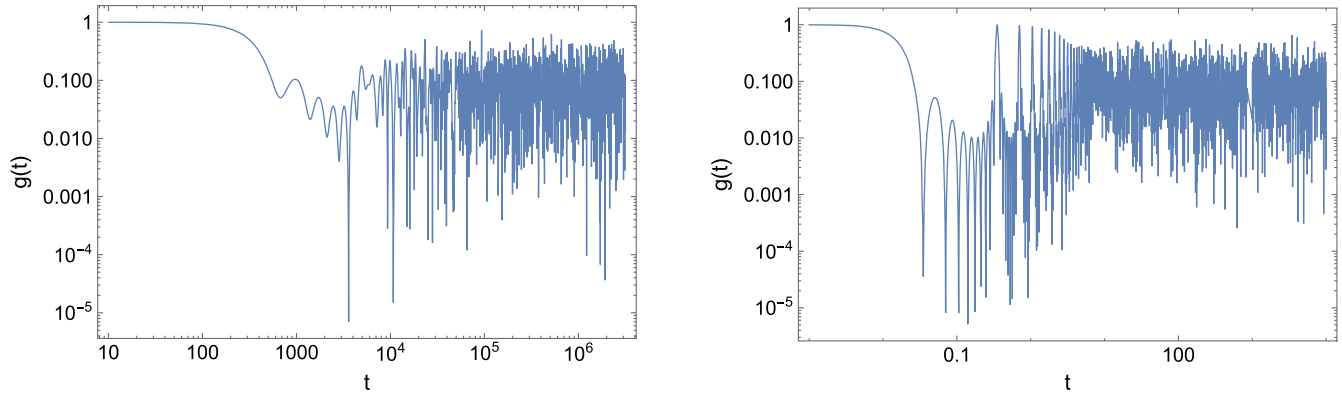


FIG. 2. This figure illustrates the SFF of the modes presented in Fig. 1, along the l-direction (left) and n-direction (right), with β fixed to zero.

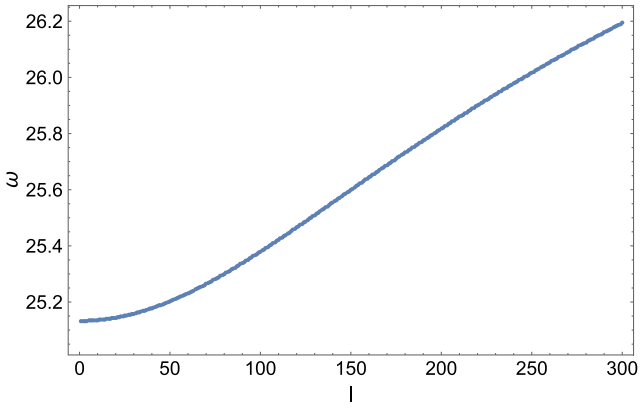


FIG. 3. Normal modes along l direction for BTZ black hole for $r_H/l = 100 \gg 1$.

where,

$$V(r) = \frac{1}{4a^2}(b^2 - 2ba' + 2a(b' - 2c)). \tag{30}$$

Though the general form of the potential is complex and not very enlightening to write down explicitly, some general observations are interesting to note. For large r, $V(r)$ behaves as,

$$\lim_{r\to\infty} V(r) = \frac{(d^2-1)+4\mu^2}{4r^2} + O\left(\frac{1}{r^4}\right); \tag{31}$$

which is always positive. As r approaches to r_H, $V(r)$ goes to $-\infty$. Additionally, there is a turning point at some $r_c > r_H$ where $V(r)$ changes sign. The general structure of $V(r)$ is depicted in Fig. 5. The Dirichlet boundary condition $\phi(r_0) = 0 = \psi(r_0)$ implies the existence of an infinite potential barrier at the location of the brick wall ($r = r_0$), represented by a red vertical line in Fig. 5. The task is then to find the bound states of this potential well. An interesting point to note is that as the angular momentum l increases, the height of the bump after the turning point also increases (see Fig. 6) which is an artifact of the presence of the angular momentum barrier. For a given r_0, we can tune l in such a way that no potential well forms, which corresponds to scattering states. These modes are not trapped from the perspective of a boundary observer due to their large angular momentum. We are not interested in those modes and only consider the bound states.

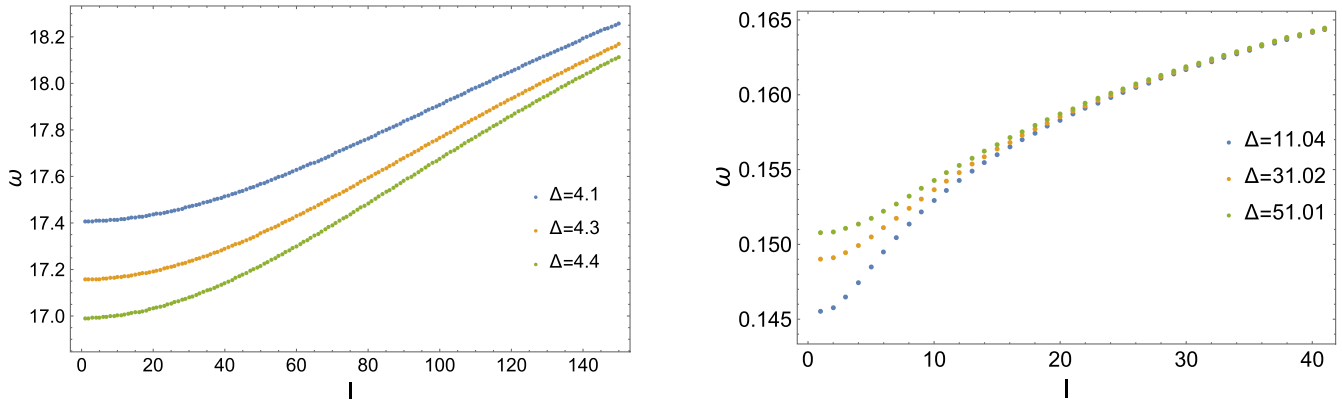


FIG. 4. Left: the Δ dependence of the normal modes along the l direction is depicted. Right: similar plots are presented for the BTZ black hole, demonstrating the Δ dependence of the normal modes along the m direction.

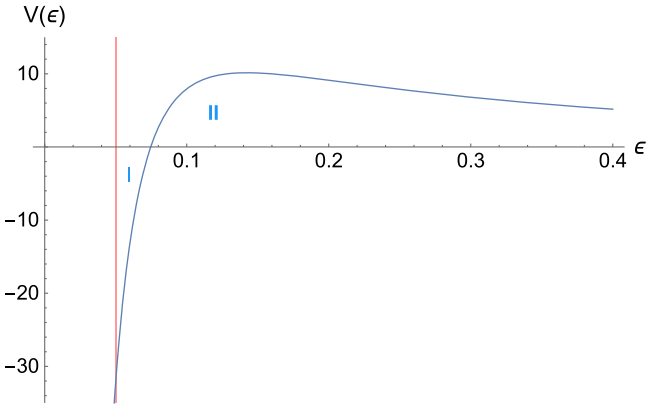


FIG. 5. Generic structure of the effective Schrödinger like potential $V(r)$ in (32). Here $l = 3$, $\omega = 0.3$, and $r_H = 1$.

The expression for $V(r)$ with $\mu = 0$ and $r_H = 1$ is given by

$$V(r) = \frac{1}{4r^2(r^4 + r^2 - 2)^2}(r^6(4l(l+2) - 4\omega^2 + 22) + (4l(l+2) - 57)r^4 - 4(2l(l+2) + 3)r^2 + 15r^8 - 4). \tag{32}$$

As shown in the Appendix (see also [43,51]), to determine the spectrum, we need the closed-form expression of $\int_{r_0}^{r_c} \sqrt{|V(r)|}$, which is not feasible for (32). However, this does not mark the end of the investigation. Interesting physics occurs when the position of the brick wall is very close to the horizon. We will further assume that the turning point is also very close to the horizon. For the second condition, we need $\frac{\omega}{l}$ not to be very large, meaning we will focus on low-lying modes for a fixed l (i.e., low n) which is also physical as long as we are in the probe limit.

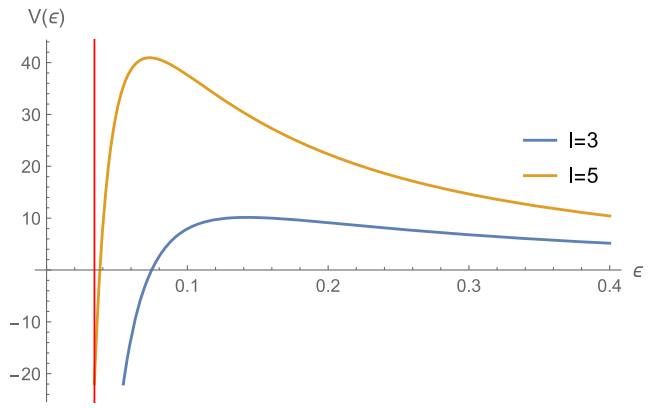


FIG. 6. Generic structure of the effective Schrödinger like potential $V(r)$ in (32). Here $l = 3$, $\omega = 0.3$, and $r_H = 1$.

The near-horizon expansion of $V(r)$ is,

$$\lim_{\epsilon \to 0} V(r = r_H + \epsilon) = V_{\text{eff}}(\epsilon) = -\frac{A_2}{\epsilon^2} + \frac{A_1}{\epsilon} - A_0 + O(\epsilon), \tag{33}$$

where $r = r_H + \epsilon$, and,

$$A_0 = \frac{7}{432}(12l(l+2) - \omega^2 - 9), \tag{34}$$

$$A_1 = \frac{18l(l+2) - 5\omega^2 + 117}{108}, \tag{35}$$

$$A_2 = \frac{9 + \omega^2}{36}. \tag{36}$$

Under the above assumption, we can approximate the original $V(r)$ by (33). A comparison of $V(\epsilon)$ and $V_{\text{eff}}(\epsilon)$ is shown in Fig. 7. With this approximation, the WKB integration can be performed exactly, yielding the following result:

$$\int_{r_0}^{r_c} |V(r)|^{\frac{1}{2}} dr = -\sqrt{A_0\epsilon_0^2 - A_1\epsilon_0 + A_2} - \frac{1}{2}\sqrt{A_2}\log\left(\frac{T_1 + 1}{T_1 - 1}\right) - \frac{A_1}{4\sqrt{A_0}}\log\left(\frac{T_2 + 1}{T_2 - 1}\right), \tag{37}$$

where,

$$T_1 = \frac{A_1\epsilon_0 - 2A_2}{2\sqrt{A_2(A_2 - A_1\epsilon_0 + A_0\epsilon_0^2)}}, \tag{38}$$

$$T_2 = \frac{-2A_0\epsilon_0 + A_1}{2\sqrt{A_0(A_2 - A_1\epsilon_0 + A_0\epsilon_0^2)}}. \tag{39}$$

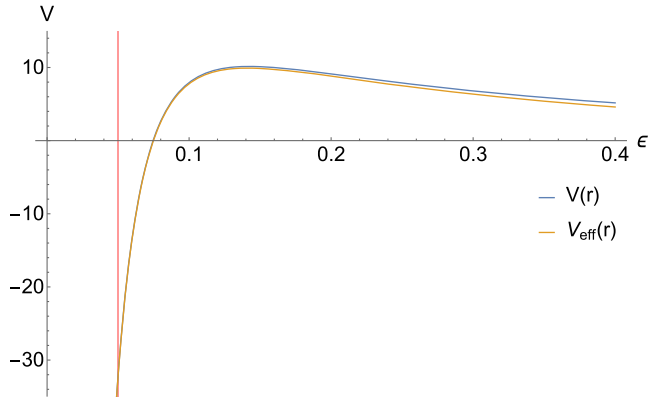


FIG. 7. Comparison of (32) and (33). This image shows that when the turning point is close to the horizon, we can approximate the WKB integration using V_{eff}. Parameters: $l = 3$, $\omega = 0.3$, and $r_H = 1$.

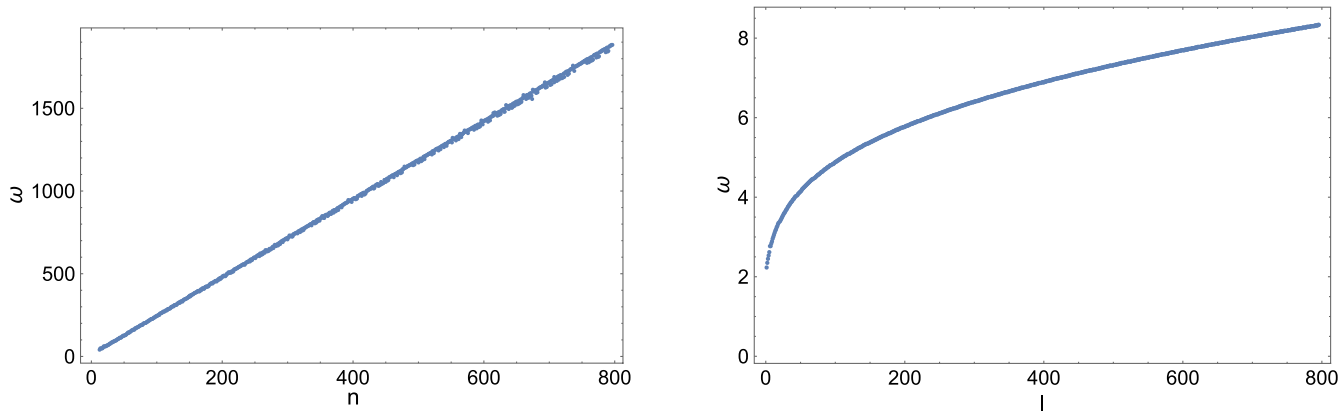


FIG. 8. Spectrum along n (left) and l (right) directions using WKB method. In the left figure, l is fixed at 5 and n starts from 10; in the right figure, n is fixed at 1 and l starts from 10. Other parameters: $r_H = 1$, $\epsilon_0 = 10^{-7.5}$.

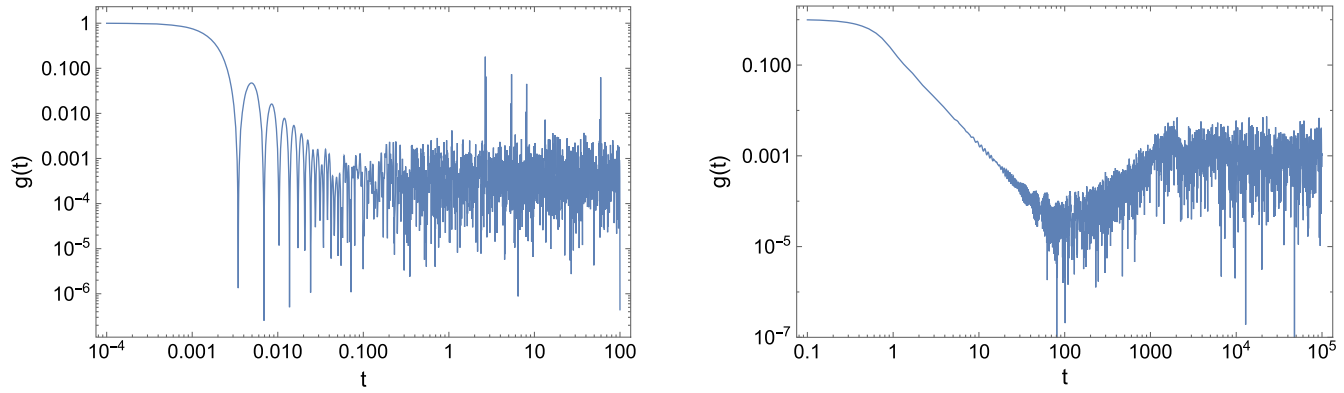


FIG. 9. SFF along n (left) and l (right) directions for the modes shown in Fig. 8. Here β is fixed to zero.

Then according to WKB method,

$$\int_{r_0}^{r_c} |V(r)|^{\frac{1}{2}} dr = \frac{3\pi}{4} + n\pi, \tag{40}$$

where n is the principal quantum number and $\epsilon_0 = r_0 - r_H$. This equation cannot be solved analytically for $\omega_{n,l}$, so we have solved it numerically for different choices of ϵ_0 using *Mathematica*. The results are the following.

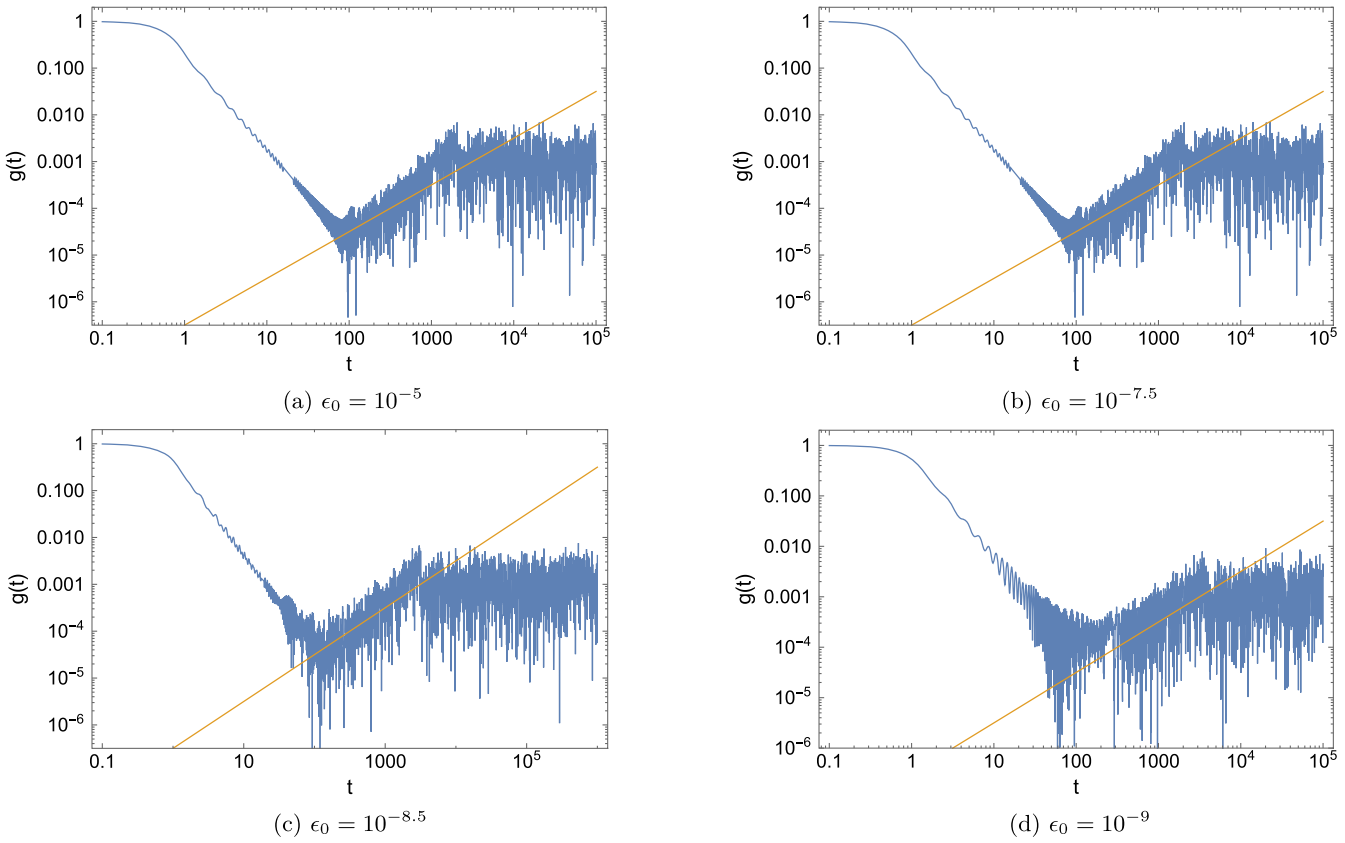
In Fig. 8, we present the spectrum along the n and l-directions. Note the striking similarity with the figures in [40]. The spectrum along n direction is linear, resembling that of a simple harmonic oscillator. Consequently, we do not observe any ramp structure in the SFF [see Fig. 9 (left)]. In contrast, the nontrivial functional dependence along l direction leads to the presence of a ramp in the SFF along l direction [see Fig. 9 (right)]. Figure 10 shows the SFFs for different ϵ_0. As ϵ_0 decreases, the slope of the ramp approaches one, consistent with our previous observation of a linear ramp in $2+1$ dimensions. In Fig. 11, we illustrate the spectrum for different values of ϵ_0. As ϵ_0 decreases, the ω values become increasingly closer to each other. This quasidegenerate property leads to the ramp observed in the SFF. Due to the instability of low-lying modes, as shown in Fig. 11, our numerical method cannot handle values of ϵ_0 below 10^{-9}.

Finally, in Fig. 12, we present the Δ-dependence of the modes along the l-direction. This behavior is the opposite of what was obtained using the Liouville CFT technique, as shown in Fig. 4 (left).

V. SOLVING HEUN EQUATION PERTURBATIVELY

In this section, we will solve the radial Heun equation using a perturbative method, as discussed in [52]. To begin, we rewrite the radial Eq. (8) in terms of a dimensionless coordinate $y = \frac{r_H^2}{r^2}$, resulting in

$$y^3(1-y^2)\frac{d}{dy}\left(\frac{1-y^2}{y}\phi'(y)\right) + \left(\frac{\hat{\omega}^2}{4}y - \frac{\hat{l}^2}{4}y(1-y^2) - \frac{\hat{\mu}^2}{4}(1-y^2)\right)\phi(y) = 0, \tag{41}$$



(a) $\epsilon_0 = 10^{-5}$ (b) $\epsilon_0 = 10^{-7.5}$

(c) $\epsilon_0 = 10^{-8.5}$ (d) $\epsilon_0 = 10^{-9}$

FIG. 10. This set of figures shows how the slope of the ramp is approaching one as we move the brick wall close to the horizon. The yellow line has slope one. The noise at the end of the spectrum is caused by the removal of the first few roots from the spectrum. n is fixed to one. Here $\beta = 0$.

where we have defined $\hat{\omega} = \omega/r_H$, $\hat{l}^2 = \frac{l(l+2)}{r_H^2}$, and $\hat{\mu} = \mu$. We choose the following ansatz for $\phi(y)$,

$$\phi(y) = y^2(1-y)^{\frac{-i\hat{\omega}}{4}}\left(\frac{1+y}{2}\right)^{-\frac{\hat{\omega}}{4}}F(y). \tag{42}$$

Substituting this into (41), we obtain

$$F''(y) + \left(\frac{3}{y} + \frac{1-i\hat{\omega}/2}{y-1} + \frac{1-\hat{\omega}/2}{y+1}\right)F'(y) + \frac{(2-(1+i)\hat{\omega}/4)^2 y - q}{y(y^2-1)}F(y) = 0, \tag{43}$$

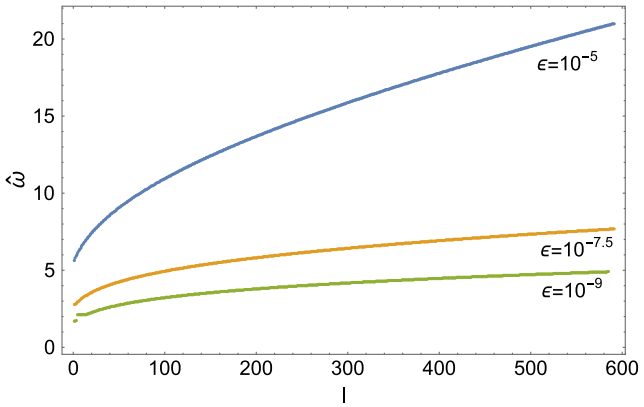


FIG. 11. Behavior of normal modes along the l direction with varying ϵ_0.

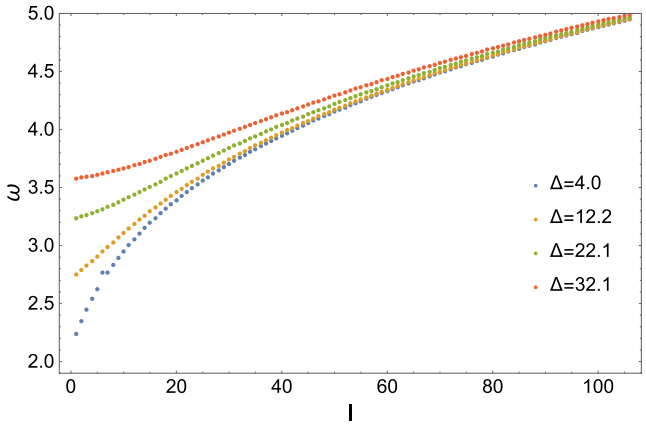


FIG. 12. Behavior of the normal modes along l-direction with varying Δ. This is opposite to the behavior observed using the Liouville CFT technique, but consistent with the results of BTZ black hole. Parameters: $r_H/l = 1$, $\epsilon_0 = 10^{-7.5}$.

where

$$q = \frac{3(i-1)}{4}\hat{\omega} - \frac{\hat{l}^2}{4} + \frac{\hat{\omega}^2}{4}. \tag{44}$$

Introducing another new variable $x = y^2$, (43) can be rewritten as

$$\begin{aligned}\mathcal{H}F(x) = {} & x(1-x)F''(x) + \frac{1}{4}((1+i)x(\omega + (-6+6i)) \\ & -(1-i)\sqrt{x}\omega + 8)F'(x) \\ & + \frac{1}{32}\left(\frac{8q}{\sqrt{x}} - i(\omega + (-4+4i))^2\right)F(x) = 0. \end{aligned} \tag{45}$$

To solve the equation perturbatively, we decompose the Hamiltonian into two terms $(\mathcal{H}_0 + \mathcal{H}_1)$ in such a way that $\mathcal{H}_1$ can be treated as a perturbation in $\hat{\omega}$

$$\begin{aligned}\mathcal{H}_0 = {} & x(1-x)\frac{d^2}{dx^2} + \left(2 - \frac{1-i}{4}\hat{\omega} - \left(3 - \frac{1+i}{4}\hat{\omega}\right)x\right)\frac{d}{dx} \\ & - \frac{1}{4}\left(\left(2 - \frac{1+i}{4}\hat{\omega})^2 - q\right)\right), \\ \mathcal{H}_1 = {} & (1-\sqrt{x})\left(\frac{1-i}{4}\hat{\omega}\frac{d}{dx} + \frac{q}{4\sqrt{x}}\right). \end{aligned} \tag{46}$$

The above decomposition has an additional benefit: $\mathcal{H}_0$ is a hypergeometric differential equation. Furthermore, we expand $F(x)$ as a perturbative series in $\hat{\omega}$.

$$F(x) = F_0(x) + F_1(x) + F_2(x)\ldots \tag{47}$$

This expansion allows us to rewrite (45) formally as

$$\begin{aligned}& (\mathcal{H}_0 + \mathcal{H}_1)(F_0 + F_1 + \ldots) = 0 \\ & \Rightarrow \mathcal{H}_0F_0 + (\mathcal{H}_0F_1 + \mathcal{H}_1F_0) + (H_0F_2 + H_1F_1) + \ldots = 0. \end{aligned}$$

At zeroth order, we have

$$\mathcal{H}_0F_0 = 0.$$

At first order

$$\begin{aligned}& \mathcal{H}_0F_1 + \mathcal{H}_1F_0 = 0 \\ & \Rightarrow F_1 = -\mathcal{H}_0^{-1}\mathcal{H}_1F_0 = -\mathcal{D}F_0. \end{aligned}$$

In second order

$$\mathcal{H}_0F_2 + \mathcal{H}_1F_1 = 0 \tag{48}$$

$$\Rightarrow F_2 = \mathcal{H}_0^{-1}\mathcal{H}_1\mathcal{H}_0^{-1}\mathcal{H}_1F_0 \tag{49}$$

$$= \mathcal{D}^2F_0. \tag{50}$$

Similarly, at the n-th order, we have, $F_n = (-1)^n\mathcal{D}^nF_0$. Thus, once F_0 is known, we can in principle construct the full perturbative series for $F(x)$.

As already mentioned earlier, at zeroth order, the radial equation reduces to a hypergeometric equation

$$x(1-x)F_0''(x) + (c - (1+a+b)x)F_0'(x) - abF_0(x) = 0, \tag{51}$$

where,

$$a, b = 1 + \frac{1}{2}\left(-\frac{1+i}{4}\hat{\omega} \pm \sqrt{q}\right), \quad c = 2 - \frac{1-i}{4}\hat{\omega}. \tag{52}$$

The solution of (51) is given in terms of hypergeometric functions

$$\begin{aligned}F_0(x) = {} & c_1{}_2F_1(a,b,c,x) \\ & + c_2x^{1-c}{}_2F_1(1+a-c, 1+b-c, 2-c, x). \end{aligned} \tag{53}$$

The near-boundary expansion of (53) is

$$F_0(x) \sim c_1 + c_2x^{1-c},$$

which implies

$$\psi \sim (1-y)^{-\frac{i\hat{\omega}}{4}}\left(\frac{1+y}{2}\right)^{-\frac{\hat{\omega}}{4}}\left(c_1y^2 + c_2y^{\frac{1-i}{2}\hat{\omega}}\right).$$

The normalizable boundary condition $(\psi \to 0)$ implies $c_2 = 0$. The near-horizon behavior of (53) is given by

$$F_0(x) \sim A + B(1-x)^{\frac{i\hat{\omega}}{2}}, \tag{54}$$

where,

$$\begin{aligned}A = {} & \frac{\Gamma(c)\Gamma(c-a-b)}{\Gamma(c-a)\Gamma(c-b)}, \\ B = {} & \frac{\Gamma(c)\Gamma(a+b-c)}{\Gamma(a)\Gamma(b)}. \end{aligned} \tag{55}$$

If we impose the Dirichlet boundary condition $F_0(x_0) = 0$ at the stretched horizon $x = x0$ (close to the event horizon) then this implies

$$\frac{A}{B} = -(1-x_0)^{\frac{i\hat{\omega}}{2}} = -\epsilon^{\frac{i\hat{\omega}}{2}} \tag{56}$$

which gives the following quantization condition

$$\mathrm{Arg}\left[\frac{\Gamma(a+b-c)\Gamma(c-a)\Gamma(c-b)}{\Gamma(c-a-b)\Gamma(a)\Gamma(b)}\right] + \frac{\hat{\omega}}{2}\log\epsilon = (2n+1)\pi, \tag{57}$$

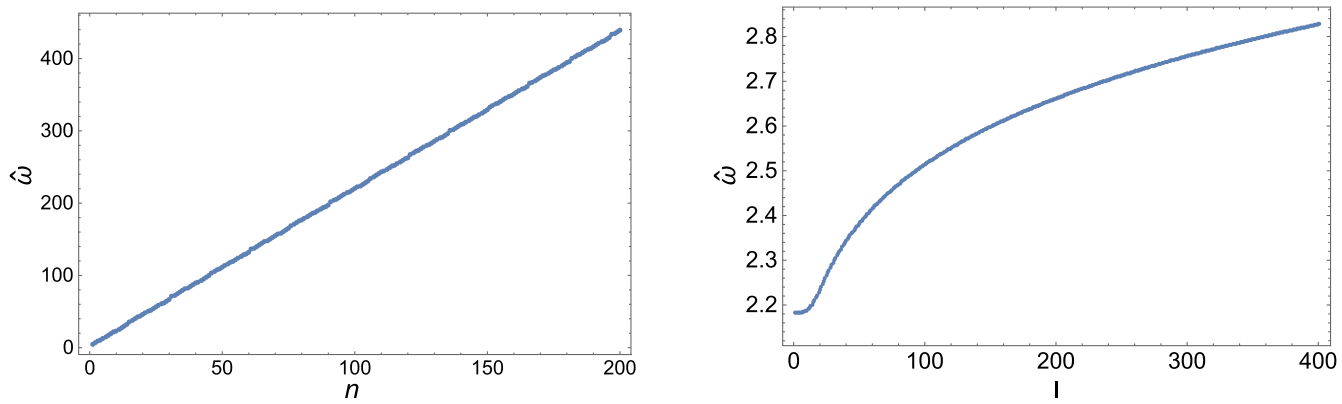


FIG. 13. Spectrum along n (left) and l (right) direction for $r_H = 10$.

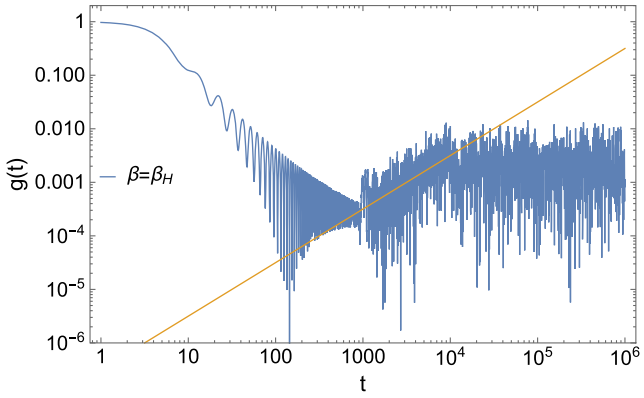


FIG. 14. SFF for the normal modes along l direction with fixed $n = 0$. Here $l_{\text{cut}} = 400$ and $\beta = \beta_H$.

where, $n \in \mathbf{Z}$. Solving this equation in *Mathematica*, we obtain ω as a function of n and l. Figure 13 shows the behavior of the spectrum in the n and l directions. As we can see again, the spectrum has a linear behavior along n and a nonlinear behavior along l. With the spectrum in hand, we can now compute the SFF. Figure 14 shows SFF along the l direction at temperature β_H which is the Hawking temperature of the black hole, but it is worth mentioning that β is nothing but a parameter here.

So far, we have discussed the zeroth-order solution. However, one can find the higher-order corrections to the normal modes by adding order-by-order corrections to the wave function. Explaining all the technical details is beyond the scope of this paper. However, a thorough discussion of this topic can be found in [52].

VI. GREEN'S FUNCTION AND EMERGING THERMALITY

A. In momentum space

In this section, we closely examine the analytic structure of the Green's function, following the approaches of [53,49]. For any asymptotic AdS geometry, the Son-Starinets [48] prescription provides a method to compute the Green's function of the boundary theory as the ratio of the normalizable and non-normalizable modes. From (23), this implies

$$G = \frac{b_{11} + R_{c_1c_2} a_{11}}{b_{22} + R_{c_1c_2} a_{22}}. \tag{58}$$

The poles of this Green's function correspond to the excitations of the system when perturbed by the boundary operator dual to the scalar field in the bulk. Since the system is in a pure state (with no infalling boundary condition), we expect the poles to lie on the real line. Except that, the function is analytic in the whole complex plane. In Fig. 15, we plot the Green's function G as a function of ω. As z_0 is decreased, i.e., as the brick wall approaches the horizon, the poles come closer together. In the limit $\epsilon_0 \to 0$, these poles are so close that we can approximate them as a branch cut. However, there is a caveat: for any given ϵ_0, there is always a maximum gap $\Delta\omega$ (noting that the spectrum is not equidistant), which sets a minimum timescale of $\sim \frac{1}{\Delta\omega}$. Beyond this timescale, a boundary observer begins to probe the discreteness of the spectrum.

In the position space correlator, the implication of this pole condensation is very interesting. To see this, let us first rewrite G as follows:

$$\begin{aligned} G &= \frac{b_{11} + R_{c_1c_2} a_{11}}{b_{22} + R_{c_1c_2} a_{22}} \\ &= \frac{\frac{b_{11}}{b_{22}} + R_{c_1c_2} \frac{a_{11}}{b_{22}}}{1 + R_{c_1c_2} \frac{a_{22}}{b_{22}}} \\ &= \frac{G_R^{\text{BH}} + R_{c_1c_2} \frac{a_{11}}{b_{22}}}{1 + R_{c_1c_2} \frac{a_{22}}{b_{22}}}, \end{aligned} \tag{59}$$

where the retarded correlator of the black hole, G_R^{BH}, is given in (19). The poles of the Green's function occur when

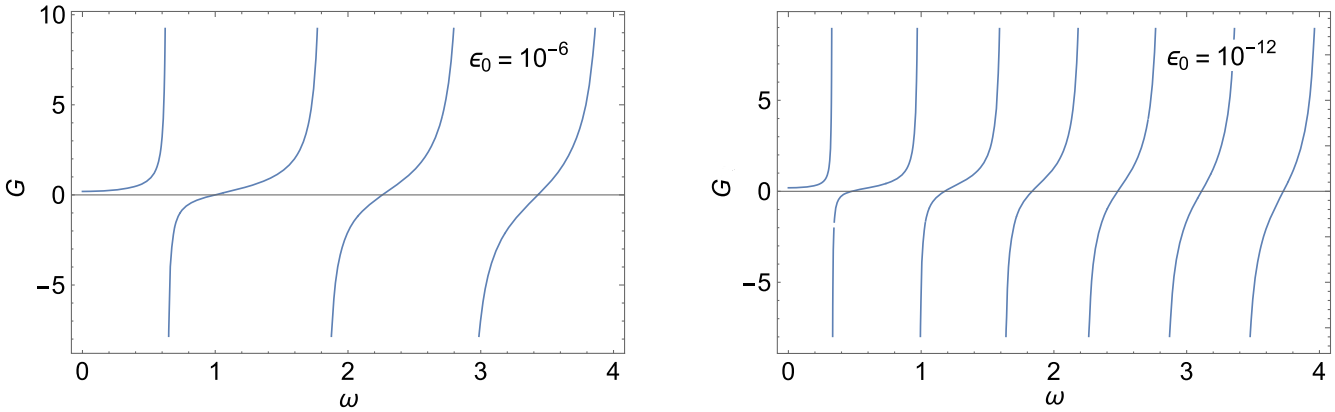


FIG. 15. Plot of Green's function, $G(\omega, l = 1)$ for two different ϵ_0. The main point to note is that as ϵ_0 decreases the poles start to accumulate on the real line.

the denominator of (59) goes to zero, which is nothing but the quantization Eq. (25). This happens because the condition: denominator $= 0$ corresponds to the vanishing of the non-normalizable mode, which is exactly the quantization condition [remember that the Dirichlet condition is already imposed in writing (23)]. The residue at these simple poles (labeled by ω_k) is given by,

$$\mathrm{Res}(G, \omega_k) = \frac{(G_R^{\mathrm{BH}} + R_{c_1 c_2} \frac{a_{11}}{b_{22}})|_{\omega=\omega_k}}{\partial_\omega (1 + R_{c_1 c_2} \frac{a_{22}}{b_{22}})|_{\omega=\omega_k}}. \tag{60}$$

Now at $\omega = \omega_k$, the denominator of (59) is zero, i.e., $R_{c_1 c_2} = -\frac{b_{22}}{b_{11}}$ which implies the numerator can be written as,

$$\begin{aligned}\left(G_R^{\mathrm{BH}} + R_{c_1 c_2} \frac{a_{11}}{b_{22}}\right)\Big|_{\omega=\omega_k} &= G_R^{\mathrm{BH}} - \frac{a_{11}}{a_{22}}\Big|_{\omega=\omega_k} \\ &= G_R^{\mathrm{BH}} - (G_R^{\mathrm{BH}})^*|_{\omega=\omega_k} \\ &= 2i\,\mathrm{Im}\, G_R^{\mathrm{BH}}(\omega, l)|_{\omega=\omega_k}, \end{aligned} \tag{61}$$

whereas the denominator becomes

$$\partial_\omega \left(1 + R_{c_1 c_2} \frac{a_{22}}{b_{22}}\right)\Big|_{\omega=\omega_k} = \partial_\omega e^{-i\theta(\omega,l)}|_{\omega=\omega_k}, \tag{62}$$

where $\theta(\omega, l)$ is given in a footnote after (25). Thus, the residue is,

$$\mathrm{Res}(G, \omega_k) = 2i \frac{\mathrm{Im}\, G_R^{\mathrm{BH}}(\omega, l)|_{\omega=\omega_k}}{\partial_\omega e^{-i\theta(\omega,l)}|_{\omega=\omega_k}}. \tag{63}$$

If a function has simple poles at $\omega_1, \omega_2, \ldots, \omega_k, \ldots$, it can be expressed as,

$$G(\omega, l) = \sum_k \left(\frac{\omega}{\omega_k}\right)^\delta \frac{\mathrm{Res}(G, \omega_k)}{\omega - \omega_k}. \tag{64}$$

[9] The additional factor is included to ensure the convergence of G on the contour as $\omega \to \infty$. When the poles are very closely spaced, the sum can be approximated by an integral, given by the following expression:

$$\begin{aligned} G(\omega, l) &= \int d\omega_k \frac{\rho_\omega(\omega_k, l)}{\omega - \omega_k} \quad \text{with} \quad \rho_\omega(\omega_k, l) \\ &= \frac{dk}{d\omega_k} \left(\frac{\omega}{\omega_k}\right)^\delta \mathrm{Res}(G, \omega_k), \end{aligned} \tag{65}$$

which implies

$$\begin{aligned} G(\omega + i\epsilon, l) - G(\omega - i\epsilon, l) &\approx \int d\omega_k \rho_\omega(\omega_k, l) 2\pi i \delta(\omega - \omega_k) \\ &= 2\pi i \rho_\omega(\omega, l). \end{aligned} \tag{66}$$

Thus, when the poles are densely packed, they can be approximated by a branch cut, with the discontinuity given by (66).

We observe a similar feature as the brick wall approaches the event horizon, allowing us to make analogous approximations for the correlator in (59). To compute the discontinuity, we evaluate

$$\begin{aligned} \frac{dk}{d\omega_k} &= \frac{1}{2\pi} \frac{d\theta(\omega_k, l)}{d\omega_k} \\ &= -\frac{1}{2\pi i} e^{i\theta(\omega_k,l)} \partial_{\omega_k} e^{-i\theta(\omega_k,l)} \\ &= -\frac{1}{2\pi i} \partial_{\omega_k} e^{-i\theta(\omega_k,l)}. \end{aligned} \tag{67}$$

[9] A dispersive representation of $G(\omega)$ has been utilized in the above expression by introducing a subtracted correlator by dividing G by ω^δ. This involves contour integration in the complex ω-plane, where the exponent δ is chosen such that the contribution from the contour at infinity vanishes as $|\omega| \to \infty$ [53].

Substituting this into the expression in (65),[10] we obtain,

$$\rho_\omega(\omega_k, l) = -\frac{1}{\pi}\left(\frac{\omega^2}{\omega_k^2}\right)^\Delta \mathrm{Im}\, G_R^{\mathrm{BH}}(\omega, l_0)\Big|_{\omega=\omega_k}. \quad (68)$$

Given the correlator in (59), we can define the retarded, Feynman, and Wightman correlators as follows:

$$G_R(\omega, l) = G(\omega + i\epsilon, l) = \sum_k \left(\frac{\omega^2}{\omega_k^2}\right)^\Delta \frac{\mathrm{Res}(G, \omega_k)}{\omega - \omega_k + i\epsilon}, \quad (69)$$

$$G_F(\omega, l) = \sum_{\omega_k>0}\left(\frac{\omega^2}{\omega_k^2}\right)^\Delta \frac{\mathrm{Res}(G, \omega_k)}{\omega - \omega_k + i\epsilon} + \sum_{\omega_k<0}\left(\frac{\omega^2}{\omega_k^2}\right)^\Delta \frac{\mathrm{Res}(G, \omega_k)}{\omega - \omega_k - i\epsilon}, \quad (70)$$

$$G_W(\omega, l) = -\mathrm{sign}\omega\, \mathrm{Im}\, G_R(\omega, l). \quad (71)$$

Thus, the imaginary part of the retarded Green's function can be expressed as

$$\mathrm{Im}\, G_R(\omega, l) = \frac{1}{2i}(G(\omega + i\epsilon, l) - G(\omega - i\epsilon, l)) = \pi\rho_\omega(\omega, l). \quad (72)$$

Substituting (68) into (72), we find,

$$\mathrm{Im}\, G_R(\omega, l) = -\mathrm{Im}\, G_R^{\mathrm{BH}}(\omega, l)|_{\omega=\omega_k}. \quad (73)$$

It is worth emphasizing that, while this equation appears simple, it encodes a very nontrivial relation. The pole structures of the two Green's functions G_R and G_R^{BH}, are fundamentally different. The Green's function G_R has poles on the real axis, which correspond to the normal modes of the system. On the other hand, G_R^{BH} has poles in the lower-half complex plane, corresponding to black hole quasi normal modes. This equation indicates that, when the real-valued poles become very dense, they can be approximated as forming a branch cut. The discontinuity across this branch cut contains information about the complex-valued quasinormal modes.

B. In position space

So far, we have discussed the momentum space Green's function. In this section, we turn our attention to the position space Green's function, focusing primarily on the Feynman propagator, which is given by[11]

$$C(u, v) = \mathcal{N}\iint dw dp e^{ipv - iwu} G_F(w, p) = \mathcal{N}\iint dw dp e^{ipv-iwu}\sum_{w_k}\left(\frac{w^2}{w_k^2}\right)^\Delta \frac{\mathrm{Res}(G, w_k)}{w - w_k \pm i\epsilon}. \quad (74)$$

Here, the $\pm$ sign corresponds to positive and negative w_k, respectively. For simplicity, we will consider $u > 0$ without loss of generality, which allows us to select only the positive w_k. After integrating over w, the expression simplifies to:

$$C(u, v) = \mathcal{N}\sum_{w_k}\int dp e^{ipv - iw_k u}\mathrm{Res}(G, w_k). \quad (75)$$

As mentioned earlier, when the brick wall is very close to the horizon, the sum over k can be approximated as an integral. In this approximation, the discrete w_k becomes a continuous variable w. Thus, the expression for $C(u, v)$ becomes[12]:

$$C(u, v) = \mathcal{N}\iint dp dw e^{ipv-iwu}\,\mathrm{Im}\, G_R^{\mathrm{BH}}(w, l) = \mathcal{N}\iint dp dw e^{ipv-iwu}(G_R^{\mathrm{BH}}(w, l) - G_R^{\mathrm{BH}}(w, l)^*). \quad (76)$$

Here, the first term has poles in the lower half-plane, while the second term has poles in the upper half-plane. Consequently, only the first term contributes, and it reproduces the exact position-space Green's function, which corresponds to that of a thermal one with a temperature equal to the Hawking temperature of the black hole.

This result implies that, although we start from a pure state, the two-point correlator can be well approximated by a thermal correlator when the brick wall is close to the horizon. Therefore, a boundary observer cannot distinguish this pure state from a thermal state unless they wait for an exceptionally long time or measure higher-point correlators.

VII. DISCUSSION

In this study, we explored a minimally coupled scalar field in the bulk five-dimensional AdS-Schwarzschild spacetime, which is dual to the gauge-invariant composite scalar operators $\mathrm{Tr}(F_{\mu\nu}F^{\mu\nu})$ or $\mathrm{Tr}(F_{\mu\nu}\tilde{F}^{\mu\nu})$ in the boundary four dimensional $\mathcal{N} = 4$ SYM theory. The scalar field was quantized using a Dirichlet boundary condition, ensuring that the scalar field vanishes on the stretched horizon, effectively imposing a perfectly reflecting boundary

[10]Also, choosing $\delta = 2\Delta$.

[11]Here u, v are the position space variables conjugate to $w = \frac{l-\omega}{2}$ and $p = \frac{l+\omega}{2}$.

[12]Here we are absorbing various numerical factors within $\mathcal{N}$ in various steps.

condition instead of the more conventional ingoing boundary condition near the horizon. This quantization results in normal modes that are real-valued, in contrast to the complex-valued quasinormal modes typically observed. These normal modes are labeled by two quantum numbers: the principal quantum number n and the angular momentum quantum number l. A significant degeneracy exists in the spectrum; for each l, there can be $(2l+1)^2$ states with the same ω which is because of spherical symmetry of the problem. Since the radial equation takes the form of a Heun equation, no exact solution is available, necessitating the use of various approximate methods to determine the normal modes. We employed techniques from Liouville CFT, as previously utilized in [46], to calculate these normal modes. The spectrum shows linearity along the n direction very similar to empty AdS normal modes. Although a nontrivial dependence is observed along the l direction. However, the corresponding single-particle SFF does not exhibit a clear ramp structure. This can be attributed to the absence of logarithmic dependence of the low-lying modes along the l-direction, a feature that was crucial in the BTZ black hole case for producing the linear ramp. Furthermore, we were unable to obtain the modes for sufficiently large quantum numbers and for small $r_H/l \geq 1$. Improving numerical methods to identify these could be beneficial, not only for SFF analysis but also for extracting black hole quasinormal modes. Insights from these modes could provide a deeper understanding of strongly coupled thermal $\mathcal{N}=4$ super Yang-Mills (SYM) theory.

We then applied the WKB method to solve the spectrum, which allowed us to easily compute the high-lying modes. Using this approach, we found that the corresponding single-particle SFF along l direction exhibits a clear dip-ramp-plateau (DRP) structure, with a linear ramp of slope one in the log-log plot (see Fig. 10). It is important to note that the spectrum is deterministic, rather than random as seen in various Gaussian ensembles while choosing the matrix elements. Despite this determinism, the slope of the ramp is one, similar to that observed in random matrix theory.[13] However, it is important to note that our numerical methods currently encounter difficulties as we approach very close to the horizon, where the numerics break down for extremely small values of the cutoff ϵ_0. It is important to note that while the SFF exhibits a distinct DRP structure, the LSD does not follow the conventional Wigner-Dyson distribution. However, by generalizing this simple boundary condition, as demonstrated in [41], one can achieve a Wigner-Dyson LSD accompanied by a linear ramp.

[13]For a comprehensive overview of deterministic sequences that exhibit a linear ramp in the SFF, see [54]. Among these, the logarithmic sequence is the simplest example, demonstrating a linear ramp with a slope of one.

We have attempted to solve the Heun equation perturbatively to determine the normal modes and the corresponding SFF. So far, we have only used the zeroth order equation to compute the normal modes. Although it is, in principle, possible to find higher-order corrections to the wave functions and normal modes, it is quite challenging in practice. Despite this, we have been able to show a linear ramp of slope *one* the SFF along l-direction.

Since chaos is closely related to thermality, we expect observing thermal behavior emerging from the system. This behavior is demonstrated by computing the Green's function and showing that the Green's function of this pure state can be approximated by the thermal retarded Green's function of $\mathcal{N}=4$ SYM at a temperature equal to the black hole's Hawking temperature. This approximation holds when the brick wall is placed very close to the horizon, where the poles of the Green's function become so densely packed that they can be approximated as a branch cut. The discontinuity around this branch cut captures the thermal correlator's information. However, over long timescales, the pole structure becomes apparent instead of the branch cut. In [38], it is suggested that this transition occurs around the Page time, approximately $O(N)$, and it would be valuable to examine this timescale by computing the gap in the spectrum. For a more detailed discussion, see [55].

The main result of this article is the clear DRP structure with a linear ramp of slope one in the single-particle SFF constructed from the normal mode spectrum along the l direction for $1 \leq r_H/L \ll \infty$. This behavior arises from the nontrivial dependence of the spectrum on l quantum number when the brick wall is placed very close to the horizon. In this limit, the retarded correlator can be effectively approximated by a thermal correlator.

There are several promising directions for future work. One avenue is to compute the normal modes for charged and rotating black holes. Another direction is to generalize this framework to fermionic or gauge fields. A particular concern is the absence of the ramp for $r_H/L \gg 1$, which is due to the nonlogarithmic dependence of the low-lying normal modes on l. In this limit, the approximation given in equation (5.13) of [50] breaks down for the low-lying modes, although it remains valid for the high-lying modes, which exhibit logarithmic dependence. Therefore, it is possible that the high-lying modes will exhibit the ramp structure in the SFF, suggesting that the part of the spectrum responsible for the ramp may change as we vary r_H/L. Further exploration of this aspect would be very interesting.

Another issue concerns the Δ-dependence of the modes depicted in Fig. 4. We do not yet have an explanation for why this behavior is reversed compared to the BTZ case. If the large redshift (with a single zero of the blackening factor at the horizon) is responsible for the Δ-dependence of the modes, there should be no reason for this reversed behavior (note that the Δ-dependence of the WKB

spectrum is similar to that observed in BTZ). Our hunch is that this behavior may be attributed to the parameter a appearing in Eq. (C3), which becomes imaginary for the low-lying modes when $r_H > L$, but remains real in the limit $r_H \ll L$. The Liouville CFT techniques are well-suited for the small t regime, i.e., $r_H \ll L$, which lies below the Hawking-Page transition point. However, in our analysis we are working in a regime where $r_H > L$, although not as extreme as the black brane case where $t = 1/2$. It is crucial to gain a better understanding of this behavior.

Additionally, an interesting open question arises from the observation in [56] that the retarded Green's function of thermal SYM exhibits branch cuts in the lower half-plane in the weak coupling limit, where the bulk picture is highly quantum. In contrast, in the strong coupling limit—which corresponds to a classical black hole geometry—the Green's function contains complex-valued poles that are identified as quasinormal modes. In our study, we observed that placing a brick wall in the geometry leads to poles that manifest as a branch cut when the wall is very close to the horizon. It is important to emphasize that these poles lie on the real axis, since there is no dissipation in the system. If, instead of imposing Dirichlet boundary conditions, we introduce some loss by using Neumann boundary conditions (a *not-so-hard* brick wall), it is conceivable that the poles could shift away from the real line, still manifesting as a branch cut when the wall is close to the horizon. We plan to investigate this issue in future work.

The linearity of the normal modes along the n direction reminds us of the $n + l$ dependence of the normal modes in empty AdS. It is precisely this linear dependence that plays a crucial role in the instability of AdS spacetime (see [57–60] for some nonexhaustive references). It would be very interesting to explore whether any analogous instability exists in the brick wall model.

In a recent work [61], the author conjectured a correspondence between the excited states of the free scalar field in this brick wall geometry and the vacuum or excited states of a CFT under modular quantization [62] (quantization with respect to the modular Hamiltonian). Additionally, in a separate study [63], it was observed that a particular class of Floquet CFT dynamics corresponds to the extended modular Hamiltonian of a subsystem between two fixed points of the dynamics, and that the near-horizon Virasoro algebra resembles the Virasoro algebra under modular quantization. These observations suggest an intriguing future direction: to test the validity of this conjecture (or a similar one) in higher dimensions—particularly in the context of AdS_5/CFT_4. In this regard, one might employ the results of [64], which generalizes the study of Floquet CFTs to $d > 2$, to investigate this question in higher dimensions.

ACKNOWLEDGMENTS

We express our sincere gratitude to Alexander Zhiboedov, Arnab Kundu, Bobby Ezhuthachan, Chethan Krishnan and Matthew Dodelson for their valuable discussions and insightful comments.

DATA AVAILABILITY

The data supporting this study's findings are available within the article.

APPENDIX A: SPECTRAL FORM FACTOR

The spectral form factor (SFF) is defined as follows:

$$\mathcal{S}(t) = \left| \frac{\mathrm{Tr}(e^{-(\beta+it)H})}{\mathrm{Tr}(e^{-\beta H})} \right|^2. \tag{A1}$$

If the energy spectrum is known, this can be rewritten as

$$\mathcal{S}(t) = \frac{\sum_n e^{-(\beta+it)E_n} \sum_{n'} e^{-(\beta-it)E_{n'}}}{(\sum_n e^{-\beta E_n})^2}. \tag{A2}$$

Instead of referencing generic facts on the SFF (see [8] for this), let us highlight some important aspects. First, when working with an infinite-dimensional Hilbert space and a known numerical spectrum, it is often impractical to sum over the entire spectrum. Instead, we can sum up to a certain cutoff, n_{cut}, and then vary n_{cut} to check whether $\mathcal{S}(t)$ remains stable.

Second, although the system is a field-theoretic one and the number of particles is not fixed, for simplicity, we will consider the SFF constructed from the single-particle partition function of the normal modes. However, it is important to keep in mind that to obtain the full information about the system, one should work with the complete multiparticle partition function (see [38], where the full multiparticle partition function is constructed for these modes).

Third, since $\vec{m}$ does not appear in the radial equation, the spectrum exhibits a large degeneracy. For each value of l, there are $(2l+1)^2$ number of modes with the same value. Consequently, the SFF becomes

$$\mathcal{S}(t) = \frac{|\sum_{n,l} (2l+1)^2 e^{-(\beta+it)E_{n,l}}|^2}{(\sum_{n,l} (2l+1)^2 e^{-\beta E_{n,l}})^2} \tag{A3}$$

Here, we will disregard these degeneracies and adopt the following definition for the SFF (symmetry resolved in some sense). The SFF along n-direction is

$$\mathcal{S}(t)|_{l,\vec{m}=\mathrm{const.}} = \frac{\sum_n e^{-(\beta+it)E_n} \sum_{n'} e^{-(\beta-it)E_{n'}}}{(\sum_n e^{-\beta E_n})^2}. \tag{A4}$$

and SFF along l-direction becomes,

$$\mathcal{S}(t)|_{n,\vec{m}=\mathrm{const.}} = \frac{\sum_{l_1} e^{-(\beta+it)E_{l_1}} \sum_{l_2} e^{-(\beta-it)E_{l_2}}}{(\sum_l e^{-\beta E_l})^2} \tag{A5}$$

In the main text, we focus on the two expressions above, which we have labeled as $g(t)$ in the various figures.

APPENDIX B: WKB APPROXIMATION METHOD

In this section, we briefly review the WKB approximation method. For simplicity, we will restrict the discussions to one dimension. We start with the Schrödinger equation for the stationary states of a single particle moving in a time-independent potential,

$$-\frac{\hbar^2}{2m}\frac{d^2\psi(x)}{dx^2}+V(x)\psi(x)=E\psi(x), \tag{B1}$$

and consider $p(x)=\sqrt{2m(E-V(x))}$. If the potential is constant, the solutions of (B1), for $E>V(x)$, are[14]

$$\psi(x)\sim A_{\pm}e^{\frac{\pm ipx}{\hbar}}.$$

However, if the potential is not constant, the solution is not as straightforward. However, we assume an ansatz for the solution as follows.

$$\psi(x)=C(x)_{\pm}e^{\frac{\pm i\phi(x)}{\hbar}}. \tag{B2}$$

Substituting (B2) into (B1) and separating the real and imaginary parts, we obtain two differential equations

$$C''(x)-C(x)\phi'(x)^2+p(x)^2C(x)=0, \tag{B3}$$

$$(C'(x)^2\phi'(x))'=0. \tag{B4}$$

The first of the two equations above cannot be solved in general. However, we assume that the amplitude $C(x)$ is slowly varying, i.e., $C''(x)$ can be neglected. Under this assumption, the equation can be solved, and in the 'classically allowed region' $(E>V(x))$, the wave function takes the following form:

$$\psi(x)=\frac{A_1}{\sqrt{p(x)}}e^{\frac{i}{\hbar}\int_x^{x^*}p(x')dx'}+\frac{B_1}{\sqrt{p(x)}}e^{-\frac{i}{\hbar}\int_x^{x^*}p(x')dx'}, \tag{B5}$$

whereas, in the classically forbidden region $(E<V(x))$, it is given by

$$\psi(x)=\frac{A_2}{\sqrt{|p(x)|}}e^{-\frac{1}{\hbar}\int_{x^*}^{x}|p(x')|dx'}+\frac{B_2}{\sqrt{|p(x)|}}e^{\frac{1}{\hbar}\int_{x^*}^{x}|p(x')|dx'}, \tag{B6}$$

where, $A_{1,2}, B_{1,2}$ are two sets of arbitrary constants that are yet to be fixed.

[14]For $E<V(x)$, the solutions would be $\psi(x)\sim B_{\pm}e^{\frac{\pm px}{\hbar}}$.

As we can see from above, there is a significant problem at the classical turning points where $E=V(x)$. At these points, both (B5) and (B6) diverge. Therefore, these points must be treated separately. The solutions at the turning points allow us to connect the constants of the solutions in (B5) and (B6), as the turning point acts as a bridge between the two regions. We assume that the potential varies slowly near the turning point such that

$$V(x)=E+V'(x^*)(x-x^*), \tag{B7}$$

where, x^* is the classical turning point which is derived by solving $V(x)=E$. If we substitute (B7) in (B1), the Schrödinger equation becomes,

$$\frac{d^2\psi(x)}{dx^2}=\zeta^3(x-x^*)\psi(x), \tag{B8}$$

with $\zeta=(\frac{2m}{\hbar^2}V'(x^*))^{1/3}$. After a change of variable, $z\equiv\zeta(x-x^*)$, the above equation takes the form of the Airy's equation

$$\frac{d^2\psi(z)}{dz^2}=z\psi(z).$$

Therefore, the solutions are given as a sum of the Airy functions

$$\psi(z)=\alpha Ai(z)+\beta Bi(z). \tag{B9}$$

Let us consider a scenario (Fig. 16) to illustrate how this method is used in practice. Assume that the potential is such that the region where $-\infty<x<x^*$ is classically forbidden (region II), and the region where $\infty>x>x^*$ is classically allowed (region I). In this case, the wave function in region I is given by (B5), and in region II, it is given by (B6). Since the asymptotic forms of both $Ai(z)$ and $Bi(z)$ are known, by matching (B9) with (B5) and (B6) in the two asymptotic regions $z\gg 0$ and $z\ll 0$ we can derive the WKB connection formulas relating the constants of the solutions $\{A_1,B_1\}$, $\{A_2,B_2\}$ and $\{\alpha,\beta\}$.

In particular, we can consider an example of the type Fig. 5 with one turning point. Then, using the normalizability condition for solution in $z\gg 0$ region, which implies $B_2=0$, one can show that the connection formulas are given by

$$A_1=-ie^{i\frac{\pi}{4}}A_2, \qquad B_1=ie^{-i\frac{\pi}{4}}A_2, \tag{B10}$$

and correspondingly the solutions in the two regions are given by

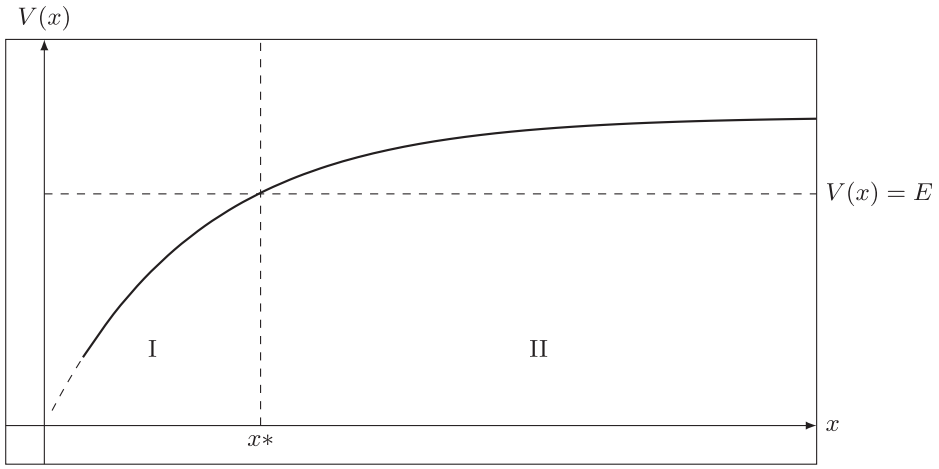


FIG. 16. Schematic diagram of a potential, illustrating the classically allowed and classically forbidden regions for a particle with energy E. The point $x*$ denotes the turning point.

$$\psi(x) = \begin{cases} \frac{2A_2}{\sqrt{p(x)}}\cos\left(\frac{1}{\hbar}\int_x^{x^*} p(x')dx' - \frac{\pi}{4}\right), & \text{for region-I} \\ \frac{A_2}{\sqrt{|p(x)|}}\exp\left(-\frac{1}{\hbar}\int_{x^*}^{x} |p(x')|dx'\right), & \text{for region-II.} \end{cases}$$

This type of potential has a cutoff at $\psi(x_0) = 0$, for some $x_0 < x^*$, then from the solution for region II, one finds that $\cos\left(\frac{1}{\hbar}\int_{x_0}^{x^*} p(x')dx' - \frac{\pi}{4}\right)$ must be zero for $\psi(x_0) = 0$, in other words, the condition

$$\frac{1}{\hbar}\int_{x_0}^{x^*} p(x')dx' = \frac{3\pi}{4} + n\pi, \quad \forall\ n \in \mathbb{Z}$$

must be satisfied.

Validity of the WKB approximation:

We will end this section by discussing the validity of the WKB approximation method. To do that, we put $\psi(x) = e^{i\frac{\phi(x)}{\hbar}}$ in (B1) and we get

$$i\hbar\phi''(x) - (\psi'(x))^2 + p(x)^2 = 0 \tag{B11}$$

Therefore, in the quasiclassical limit one would expect

$$|\hbar\phi''(x)| \ll (\psi'(x))^2$$
$$or, \left|\frac{d}{dx}\left(\frac{\hbar}{\phi'(x)}\right)\right| \ll 1$$

Since, from (B3) we know that $\phi'(x) = p(x)$ we can write the condition as

$$\left|\frac{d}{dx}\left(\frac{\hbar}{p(x)}\right)\right| \ll 1 \tag{B12}$$

From the above equation, we can see that, at the classical turning point, the condition does not hold since $p(x) = 0$, as we mentioned earlier also.

APPENDIX C: CONNECTION FORMULAS

Following the connection formulas given in [45,65], the incoming and outgoing modes near the horizon can be written in terms of the normalizable and non-normalizable modes near the boundary as

$$\begin{aligned}\chi_+^{(\tilde{t})} = \sum_{\theta'=\pm}&(M_{++}(a_{\tilde{t}}, a; a_0)M_{-\theta'}(a, a_1; a_\infty)\tilde{t}^a e^{-\frac{1}{2}\partial_a F} \\ &+ M_{+-}(a_{\tilde{t}}, a; a_0)M_{+\theta'}(a, a_1; a_\infty)\tilde{t}^{-a} e^{\frac{1}{2}\partial_a F})\tilde{t}^{\frac{1}{2}-a_0+a_{\tilde{t}}} \\ &\times (1-\tilde{t})^{a_t - a_1} e^{\frac{1}{2}(\partial_{a_{\tilde{t}}} + \theta'\partial_{a_1})F}\chi_{\theta'}^{(1)}\end{aligned} \tag{C1}$$

and

$$\begin{aligned}\chi_-^{(\tilde{t})} = \sum_{\theta'=\pm}&(M_{-+}(a_{\tilde{t}}, a; a_0)M_{-\theta'}(a, a_1; a_\infty)\tilde{t}^a e^{-\frac{1}{2}\partial_a F} \\ &+ M_{+-}(a_{\tilde{t}}, a; a_0)M_{+\theta'}(a, a_1; a_\infty)\tilde{t}^{-a} e^{\frac{1}{2}\partial_a F})\tilde{t}^{\frac{1}{2}-a_0+a_{\tilde{t}}} \\ &\times (1-\tilde{t})^{a_{\tilde{t}} - a_1} e^{\frac{1}{2}(\partial_{a_{\tilde{t}}} + \theta'\partial_{a_1})F}\chi_{\theta'}^{(1)}\end{aligned} \tag{C2}$$

where,

$$M_{\theta\theta'}(\alpha, \beta; \gamma) = \frac{\Gamma(-2\theta'\beta)\Gamma(1+2\theta\alpha)}{\Gamma(\frac{1}{2}+\theta\alpha-\theta'\beta+\gamma)\Gamma(\frac{1}{2}+\theta\alpha-\theta'\beta-\gamma)} \tag{C3}$$

$$F(\tilde{t}) = \frac{(\frac{1}{4}-a^2-a_1^2+a_\infty^2)(\frac{1}{4}-a^2-a_{\tilde{t}}^2+a_0^2)\tilde{t}}{\frac{1}{2}-2a^2} \tag{C4}$$

$$a^2 = \left(-\frac{1}{4} - u + a_{\tilde{t}}^2 + a_0^2\right)\left(1 - \frac{(-1+2a_0^2+2a_1^2-2a_\infty^2+2a_{\tilde{t}}^2-2u)(-1+4a_{\tilde{t}}^2-2u)}{2(-1+4a_0^2+4a_{\tilde{t}}^2-4u)(-1+2a_0^2+2a_{\tilde{t}}^2-2u)}\tilde{t}\right)^2 \tag{C5}$$

In the above, we used the expansion of the conformal block F in the parameter t [45], retaining only the leading-order term. The values of the parameters depend on the specific space-time that we are considering. For the AdS-Schwarzschild black hole, the parameters are [65]

$$\tilde{t} = \frac{r_h^2}{2r_h^2+1} \tag{C6}$$

$$a_{\tilde{t}} = \frac{i\omega}{2}\frac{r_h}{2r_h^2+1} \tag{C7}$$

$$a_1 = \frac{\Delta-2}{2} \tag{C8}$$

$$a_0 = 0 \tag{C9}$$

$$a_\infty = \frac{\omega}{2}\frac{\sqrt{r_h^2+1}}{2r_h^2+1} \tag{C10}$$

$$u = -\frac{l(l+2)+2(2r_h^2+1)+r_h^2\Delta(\Delta-4)}{4(r_h^2+1)} + \frac{r_h^2}{4(1+r_h^2)}\frac{\omega^2}{2r_h^2+1} \tag{C11}$$

Substituting (C1) and (C2) in (14), we extract the parameters a_{11}, a_{22}, b_{11}, and b_{22} to be

$$\begin{aligned}
a_{11} &= [M_{++}(a_{\tilde{t}},a;a_0)M_{-+}(a,a_1;a_\infty)\tilde{t}^a e^{-\frac{1}{2}\partial_a F} \\
&\quad + M_{+-}(a_{\tilde{t}},a;a_0)M_{++}(a,a_1;a_\infty)\tilde{t}^{-a}e^{\frac{1}{2}\partial_a F}] \\
&\quad \times \tilde{t}^{\frac{1}{2}-a_0+a_{\tilde{t}}}(1-\tilde{t})^{a_t-a_1}e^{-\frac{1}{2}(\partial_{a_{\tilde{t}}}+\partial_{a_1})F} \\
a_{22} &= [M_{++}(a_{\tilde{t}},a;a_0)M_{--}(a,a_1;a_\infty)\tilde{t}^a e^{-\frac{1}{2}\partial_a F} \\
&\quad + M_{+-}(a_{\tilde{t}},a;a_0)M_{+-}(a,a_1;a_\infty)\tilde{t}^{-a}e^{\frac{1}{2}\partial_a F}] \\
&\quad \times \tilde{t}^{\frac{1}{2}-a_0+a_{\tilde{t}}}(1-\tilde{t})^{a_{\tilde{t}}-a_1}e^{-\frac{1}{2}(\partial_{a_{\tilde{t}}}-\partial_{a_1})F} \\
b_{11} &= [M_{-+}(a_{\tilde{t}},a;a_0)M_{-+}(a,a_1;a_\infty)\tilde{t}^a e^{-\frac{1}{2}\partial_a F} \\
&\quad + M_{--}(a_{\tilde{t}},a;a_0)M_{++}(a,a_1;a_\infty)\tilde{t}^{-a}e^{\frac{1}{2}\partial_a F}] \\
&\quad \times \tilde{t}^{\frac{1}{2}-a_0-a_t}(1-\tilde{t})^{a_{\tilde{t}}-a_1}e^{-\frac{1}{2}(\partial_{a_{\tilde{t}}}+\partial_{a_1})F} \\
b_{22} &= [M_{-+}(a_{\tilde{t}},a;a_0)M_{--}(a,a_1;a_\infty)\tilde{t}^a e^{-\frac{1}{2}\partial_a F} \\
&\quad + M_{--}(a_{\tilde{t}},a;a_0)M_{+-}(a,a_1;a_\infty)\tilde{t}^{-a}e^{\frac{1}{2}\partial_a F}] \\
&\quad \times \tilde{t}^{\frac{1}{2}-a_0-a_{\tilde{t}}}(1-\tilde{t})^{a_{\tilde{t}}-a_1}e^{-\frac{1}{2}(\partial_{a_{\tilde{t}}}-\partial_{a_1})F}
\end{aligned} \tag{C12}$$

Substituting the parameters for AdS-Schwarzchild black hole (C3)–(C11) in (C12), one can check that the ratio of the parameters $\frac{b_{22}}{a_{22}}$ can be written as

$$\frac{b_{22}}{a_{22}} = (\tilde{t})^{-iQ}\frac{\Lambda}{\Lambda^*} \tag{C13}$$

where,

$$\begin{aligned}
\tilde{t} &= \frac{r_h^2}{2r_h^2+1}, \qquad Q = \frac{r_h\omega}{2r_h^2+1}, \\
\Lambda &= \Gamma(1-iQ)\left(e^{P_1}R_1\Gamma\left(\frac{1}{2}-a-iQ\right)^2\right. \\
&\quad \left. + e^{P_2}R_2\Gamma\left(\frac{1}{2}+a-iQ\right)^2\right),
\end{aligned}$$

$$\begin{aligned}
P_1 &= \frac{a}{(1-4a^2)^2}\left(-4a^2+\frac{r_h^2\omega^2}{(2r_h^2+1)^2}+1\right) \\
&\quad \times\left(-4a^2-(\Delta-2)^2+\frac{(r_h^2+1)\omega^2}{(2r_h^2+1)^2}+1\right),
\end{aligned}$$

$$\begin{aligned}
R_1 &= \Gamma(2a)\Gamma(2a+1)\Gamma\left(\frac{1}{2}\left(-2a+\Delta-\frac{\sqrt{r_h^2+1}\omega}{2r_h^2+1}-1\right)\right) \\
&\quad \times\Gamma\left(\frac{1}{2}\left(-2a+\Delta+\frac{\omega\sqrt{r_h^2+1}}{2r_h^2+1}-1\right)\right),
\end{aligned}$$

$$\begin{aligned}
P_2 &= \frac{a}{(4a^2-1)(2r_h^2+1)}(8a^2(r_h^2+1)+\Delta^2-4\Delta \\
&\quad +2(\Delta^2-4\Delta+2)r_h^2-\omega^2+2),
\end{aligned}$$

$$\begin{aligned}
R_2 &= \Gamma(-2a)\Gamma(1-2a)\Gamma\left(\frac{1}{2}\left(2a+\Delta-\frac{\sqrt{r_h^2+1}\omega}{2r_h^2+1}-1\right)\right) \\
&\quad \times\Gamma\left(\frac{1}{2}\left(2a+\Delta+\frac{\omega\sqrt{r_h^2+1}}{2r_h^2+1}-1\right)\right).
\end{aligned}$$

Therefore, from (C13), it is clear that $|\frac{b_{22}}{a_{22}}| = 1$.

[1] M. Gutzwiller, *Chaos in Classical and Quantum Mechanics* (Springer, New York, 1991).
[2] J. Doe, J. Quantum Phys. **15**, 123 (1980).
[3] M. V. Berry, Proc. R. Soc. London **413**, 183 (1987).
[4] M. V. Berry, J. Phys. A **10**, 2083 (1977).
[5] A. I. Larkin and Y. N. Ovchinnikov, Sov. J. Exp. Theor. Phys. **28**, 1200 (1969).
[6] J. Maldacena, S. H. Shenker, and D. Stanford, J. High Energy Phys. 08 (2016) 106.
[7] E. Brézin and S. Hikami, Phys. Rev. E **55**, 4067 (1997).
[8] J. S. Cotler, G. Gur-Ari, M. Hanada, J. Polchinski, P. Saad, S. H. Shenker, D. Stanford, A. Streicher, and M. Tezuka, J. High Energy Phys. 05 (**2017**) 118; 09 (2018) 2.
[9] E. P. Wigner, Math. Proc. Cambridge Philos. Soc. **47**, 790 (1951).
[10] F. J. Dyson, J. Math. Phys. (N.Y.) **3**, 140 (1962).
[11] J. M. Deutsch, Rep. Prog. Phys. **81**, 082001 (2018).
[12] M. Srednicki, J. Phys. A **32**, 1163 (1999).
[13] V. Balasubramanian, B. Czech, V. E. Hubeny, K. Larjo, M. Rangamani, and J. Simon, Gen. Relativ. Gravit. **40**, 1863 (2008).
[14] J. M. Maldacena, Adv. Theor. Math. Phys. **2**, 231 (1998).
[15] J. M. Maldacena, J. High Energy Phys. 04 (2003) 021.
[16] J. L. F. Barbon and E. Rabinovici, J. High Energy Phys. 11 (2003) 047.
[17] Y. Sekino and L. Susskind, J. High Energy Phys. 10 (2008) 065.
[18] M. Van Raamsdonk, Gen. Relativ. Gravit. **42**, 2323 (2010).
[19] S. H. Shenker and D. Stanford, J. High Energy Phys. 03 (2014) 067.
[20] J. Maldacena and L. Susskind, Fortschr. Phys. **61**, 781 (2013).
[21] L. Susskind, Fortschr. Phys. **64**, 24 (2016); **64**, 44(A) (2016).
[22] A. Almheiri, X. Dong, and D. Harlow, J. High Energy Phys. 04 (2015) 163.
[23] S. D. Mathur, Classical Quantum Gravity **26**, 224001 (2009).
[24] A. Almheiri, D. Marolf, J. Polchinski, and J. Sully, J. High Energy Phys. 02 (2013) 062.
[25] S. W. Hawking, Commun. Math. Phys. **43**, 199 (1975); **46**, 206(E) (1976).
[26] S. W. Hawking, Phys. Rev. D **14**, 2460 (1976).
[27] G. Penington, J. High Energy Phys. 09 (2020) 002.
[28] A. Almheiri, N. Engelhardt, D. Marolf, and H. Maxfield, J. High Energy Phys. 12 (**2019**) 063.
[29] O. Lunin and S. D. Mathur, Nucl. Phys. **B610**, 49 (2001).
[30] S. D. Mathur, Fortschr. Phys. **53**, 793 (2005).
[31] I. Bena and N. P. Warner, Lect. Notes Phys. **755**, 1 (2008).
[32] S. D. Mathur, arXiv:1401.4097.
[33] V. S. Rychkov, J. High Energy Phys. 01 (2006) 063.
[34] C. Krishnan and A. Raju, J. High Energy Phys. 06 (2015) 054.
[35] I. Bena, E. J. Martinec, S. D. Mathur, and N. P. Warner, arXiv:2204.13113.
[36] S. Raju and P. Shrivastava, Phys. Rev. D **99**, 066009 (2019).
[37] G. 't Hooft, Nucl. Phys. **B256**, 727 (1985).
[38] V. Burman, S. Das, and C. Krishnan, J. High Energy Phys. 03 (2024) 014.
[39] E. B. Rozenbaum, L. A. Bunimovich, and V. Galitski, Phys. Rev. Lett. **125**, 014101 (2020).
[40] S. Das, C. Krishnan, A. P. Kumar, and A. Kundu, J. High Energy Phys. 01 (2023) 153.
[41] S. Das, S. K. Garg, C. Krishnan, and A. Kundu, J. High Energy Phys. 10 (2023) 031.
[42] Y. Chen, H. W. Lin, and S. H. Shenker, SciPost Phys. **18**, 072 (2025).
[43] S. Das and A. Kundu, J. High Energy Phys. 02 (2024) 049.
[44] G. Festuccia and H. Liu, J. High Energy Phys. 04 (2006) 044.
[45] G. Bonelli, C. Iossa, D. Panea Lichtig, and A. Tanzini, Commun. Math. Phys. **397**, 635 (2023).
[46] M. Dodelson, A. Grassi, C. Iossa, D. Panea Lichtig, and A. Zhiboedov, SciPost Phys. **14**, 116 (2023).
[47] H. F. Jia and M. Rangamani, J. High Energy Phys. 12 (2024) 047.
[48] D. T. Son and A. O. Starinets, J. High Energy Phys. 09 (2002) 042.
[49] S. Banerjee, S. Das, M. Dorband, and A. Kundu, Phys. Rev. D **109**, 126020 (2024).
[50] C. Krishnan and P. S. Pathak, J. High Energy Phys. 03 (2024) 162.
[51] I. Bena, P. Heidmann, R. Monten, and N. P. Warner, SciPost Phys. **7**, 063 (2019).
[52] S. Musiri and G. Siopsis, Phys. Lett. B **563**, 102 (2003).
[53] S. Giusto, C. Iossa, and R. Russo, J. High Energy Phys. 10 (2023) 050.
[54] S. Das, S. K. Garg, C. Krishnan, and A. Kundu, J. High Energy Phys. 01 (2024) 172.
[55] S. Banerjee, S. Das, A. Kundu, and M. Sittinger, J. High Energy Phys. 07 (2025) 239.
[56] S. A. Hartnoll and S. P. Kumar, J. High Energy Phys. 12 (2005) 036.
[57] P. Bizon and A. Rostworowski, Phys. Rev. Lett. **107**, 031102 (2011).
[58] O. Evnin and C. Krishnan, Phys. Rev. D **91**, 126010 (2015).
[59] O. Evnin and R. Nivesvivat, J. High Energy Phys. 01 (2016) 151.
[60] O. Evnin, Classical Quantum Gravity **38**, 203001 (2021).
[61] S. Das, J. High Energy Phys. 11 (2024) 033.
[62] T. Tada, J. Phys. A **53**, 255401 (2020).
[63] S. Das, B. Ezhuthachan, S. Porey, and B. Roy, arXiv: 2406.10899.
[64] D. Das, S. R. Das, A. Kundu, and K. Sengupta, J. High Energy Phys. 09 (2024) 095.
[65] A. Bhatta, S. Chakrabortty, T. Mandal, and A. Maurya, J. High Energy Phys. 11 (**2023**) 156.